The Mesozoic Along-Strike Tectonometamorphic Segmentation of Longmen Shan (Eastern Tibetan Plateau)

L. Airaghi, J. de Sigoyer, S. Guillot, A. Robert, J. Warren, D. Deldicque

To cite this version:

L. Airaghi, J. de Sigoyer, S. Guillot, A. Robert, J. Warren, et al.. The Mesozoic Along-Strike Tectonometamorphic Segmentation of Longmen Shan (Eastern Tibetan Plateau). Tectonics, 2018, 37 (12), pp.4655-4678. 10.1029/2018TC005005 . insu-02124485

HAL Id: insu-02124485
https://insu.hal.science/insu-02124485v1

AGU100 ADVANCING EARTH AND SPACE SCIENCE

Tectonics

RESEARCH ARTICLE
10.1029/2018TC005005

Special Section:
Ten years after the Wenchuan earthquake: new insights into the geodynamics of the eastern Tibet

Key Points:
- Metamorphic jumps of ~150 °C, 5 kbar and ~50 °C, 3 kbar are observed across the Wenchuan and Beichuan faults, respectively
- *P-T-t* conditions for the southern Longmen Shan, lower than for central Longmen Shan, do not exceed 395 °C and 6 ± 2 kbar (at 80–33 Ma)
- Different segments of the Longmen Shan underwent different tectonometamorphic evolution since the Mesozoic

Supporting Information:
- Supporting Information S1
- Table S1

Correspondence to:
L. Airaghi,
laura.airaghi@upmc.fr

Citation:
Airaghi, L., de Sigoyer, J., Guillot, S., Robert, A., Warren, C. J., & Deldicque, D. (2018). The Mesozoic along-strike tectonometamorphic segmentation of Longmen Shan (eastern Tibetan plateau). *Tectonics*, *37*, 4655–4678. https://doi.org/10.1029/2018TC005005

Received 30 JAN 2018
Accepted 12 NOV 2018
Accepted article online 14 NOV 2018
Published online 18 DEC 2018

The Mesozoic Along-Strike Tectonometamorphic Segmentation of Longmen Shan (Eastern Tibetan Plateau)

L. Airaghi[1,2], J. de Sigoyer[1], S. Guillot[1], A. Robert[3], C. J. Warren[4], and D. Deldicque[5]

[1]ISTerre, Université Grenoble Alpes, Université Savoie Mont Blanc, CNRS, IRD, IFSTTAR, Grenoble, France, [2]Now at ISTeP, Sorbonne Université, Paris, France, [3]Laboratoire Geosciences Environnement Toulouse, UMR 5563 CNRS/UR 234 IRD/UPS, Toulouse, France, [4]School of Environment, Earth and Ecosystem Sciences, The Open University, Milton Keynes, UK, [5]ENS, Laboratoire de Géologie, Paris, France

Abstract The Longmen Shan belt (eastern border of the Tibetan plateau) constitutes a tectonically active region as demonstrated by the occurrence of the unexpected 2008 M_w 7.9 Wenchuan and 2013 M_w 6.6 Lushan earthquakes in the central and southern parts of the belt, respectively. These events revealed the necessity of a better understanding of the long-term geological evolution of the belt and its effect on the present dynamics and crustal structure. New structural and thermobarometric data offer a comprehensive data set of the paleotemperatures across the belt and *P-T* estimates for low-grade metamorphic domains. In the central Longmen Shan, two metamorphic jumps of 150–200 °C, 5–6 kbar and ~50 °C, 3–5 kbar acquired during the Early Mesozoic are observed across the Wenchuan and Beichuan faults, respectively, attesting to their thrusting movement and unrevealing a major decollement between the allochtonous Songpan-Garze metasedimentary cover (at $T > 500$ °C) and the autochtonous units and the basement ($T < 400$ °C). In the southern Longmen Shan, the only greenschist facies metamorphism is observed both in the basement (360 ± 30 °C, 6 ± 2 kbar) and in the metasedimentary cover (350 ± 30 °C, 3 ± 1 kbar). Peak conditions were reached at ca. 80–60 Ma in the basement and ca. 55–33 Ma in the cover, ca. 50 Ma after the greenschist facies metamorphic overprint observed in the central Longmen Shan (ca. 150–120 Ma). This along-strike metamorphic segmentation coincides well with the present fault segmentation and reveals that the central and southern Longmen Shan experienced different tectonometamorphic histories since the Mesozoic.

1. Introduction

The Longmen Shan (LMS) thrust belt constitutes the eastern border of the Tibetan plateau (Figures 1a and 1b), a tectonically active region as demonstrated by the occurrence of the M_w 7.9 Wenchuan (2008) and M_w 6.6 Lushan (2013) earthquakes in the central and southern parts of the belt, respectively. The belt sits between the Sichuan basin to the east, which lies on the South China craton (e.g., Jiang & Jin, 2005; Huang et al., 2014) and the Songpan-Garze (SPG) block to the west and is structured along different NE-SW oriented, northwest dipping fault zones. In the central LMS, the three major faults classically identified are as follows (from the west to the east): the Wenchuan fault (WF) that lies in the Wenchuan Shear zone (WSZ), the Beichuan and the Guanxian faults (BF and GF; Figures 1 and 2). The WF and BF are thought to be inherited from the Paleozoic, when the South China block represented a passive margin (Burchfiel et al., 1995; Chen & Wilson, 1995; Roger et al., 2010) structured in tilted blocks (Jia et al., 2006). In the southern LMS, the Wulong and the Xiaoguanzi faults are often considered as the southern prolongation of the WF and BF, respectively (e.g., Cook et al., 2013; Tian et al., 2016), while the Shuangshi fault has been proposed to be the continuity of the GF (Lichun et al., 2014; Figures 1b–1d).

The WF separates the SPG units from the LMS sensu stricto. Seismic investigations show that the SPG crust west of the WF is over thickened (>60 km, Figure 1d) compared to the South China crust (~40 km, Robert, Zhu, et al., 2010; Z. Zhang et al., 2009, 2010). The timing and modality of the crustal thickening, however, still remain debated. Low-temperature thermochronology data obtained on the Pengguan, Baoxing, Xuelongbao, and Tonghua crystalline massifs (slices of the South China basement) document a phase of exhumation of the belt since ca. 30 Ma (Godard et al., 2009; Kirby et al., 2002; Tan et al., 2017; Wang et al., 2012). The shortening accommodated since the Oligocene has been estimated at ~35 km at the front of the LMS (Hubbard & Shaw, 2009; Hubbard et al., 2010). Although this value is likely to be a minimal

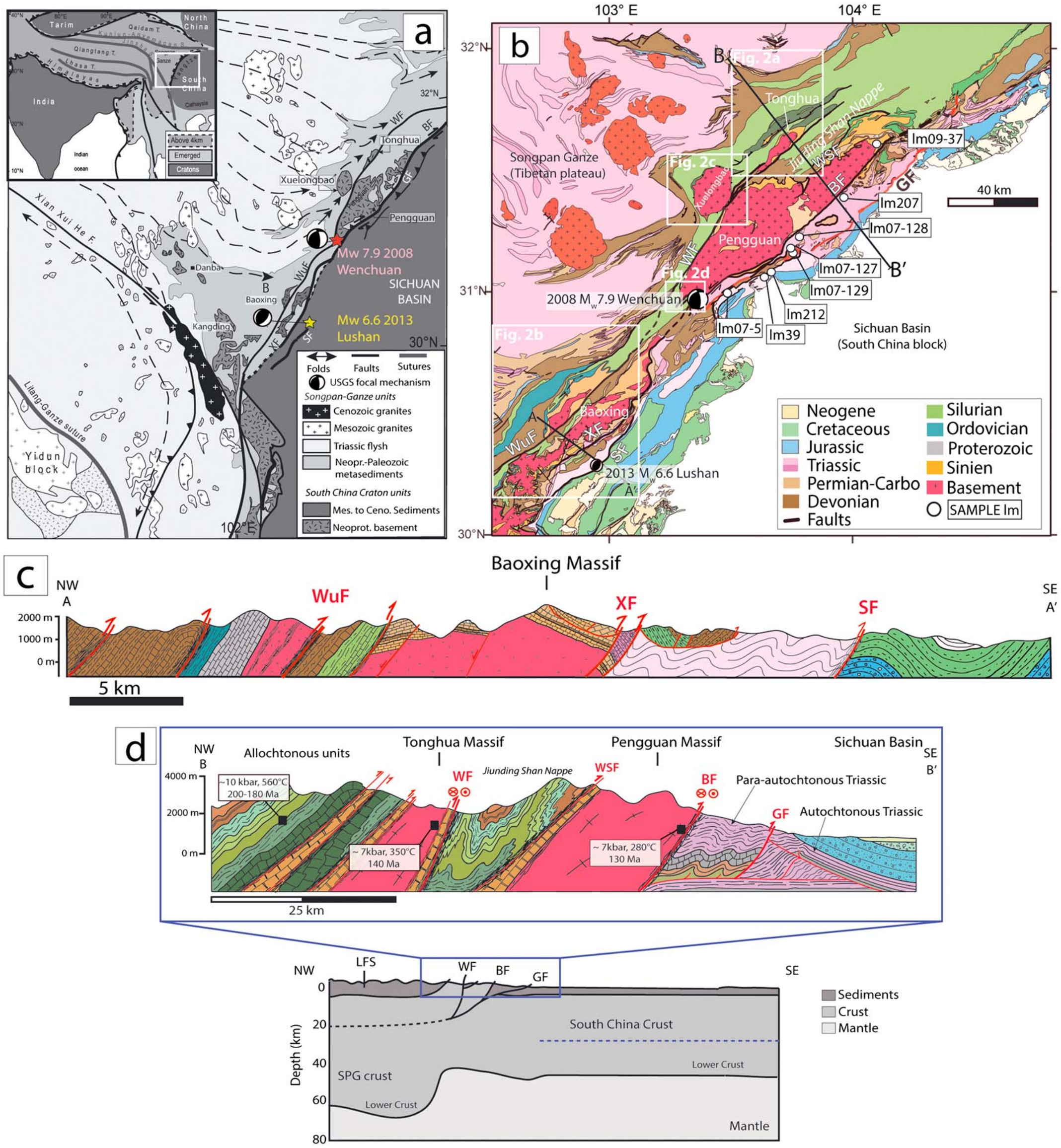

Figure 1. Structural and geological map of the Longmen Shan area. (a) Simplified geological map of the eastern border of the Tibetan plateau, modified from Billerot et al. (2017). WF: Wenchuan fault, WSF: Western Slope fault, BF: Beichuan fault, GF: Guanxian fault, WuF: Wulong fault, XF: Xiaoguanzi fault, SF: Shuangshi fault. White frame: zoom of panel b. (b) Geological map of the central Longmen Shan modified from Cook et al. (2013) and adapted from 1:200,000 geologic map (SBGMR (Sichuan Bureau of Geology and Mineral Resources), 1991). White frames: enlarged views in Figure 2. White dots: samples collected to complete transects of Figure 2 (see text for details). (c) Geological cross section along the profile AA′ for the southern Longmen Shan, modified from Cook et al. (2013). (d) Geological cross section along the profile BB′ for the central Longmen Shan. *P-T-t* conditions in frames are from Airaghi, Lanari, et al. (2017), Airaghi, de Sigoyer, et al. (2017), and Airaghi et al. (2018). The crustal structure is from the receiver function data of Robert, Pubellier, et al. (2010). USGS = United States Geological Survey.

estimate due to the propagation of blind thrusts into the Sichuan basin and to the oblique component of the BF imaged after the Wenchuan earthquake (e.g., de Michele et al., 2010), it cannot explain the total crustal thickness observed in the SPG (e.g., Robert, Pubellier, et al., 2010).

An increasing number of studies propose that part of the crustal thickness of the SPG terrane and of the central and southern Tibetan plateau is acquired during the Mesozoic (e.g., Airaghi, Lanari, et al., 2017; Airaghi, de Sigoyer, et al., 2017; Billerot et al., 2017; Kapp et al., 2003, 2007; de Sigoyer et al., 2014; Xue et al., 2017). Metamorphic and structural studies carried out in the Danba area (~ 00 km west of the LMS) and in the central LMS (Airaghi, Lanari, et al., 2017; Billerot et al., 2017; Dirks et al., 1994; Harrowfield & Wilson, 2005; Weller et al., 2013; Worley & Wilson, 1996) as well as ^{40}Ar/^{39}Ar ages on clay mineral in

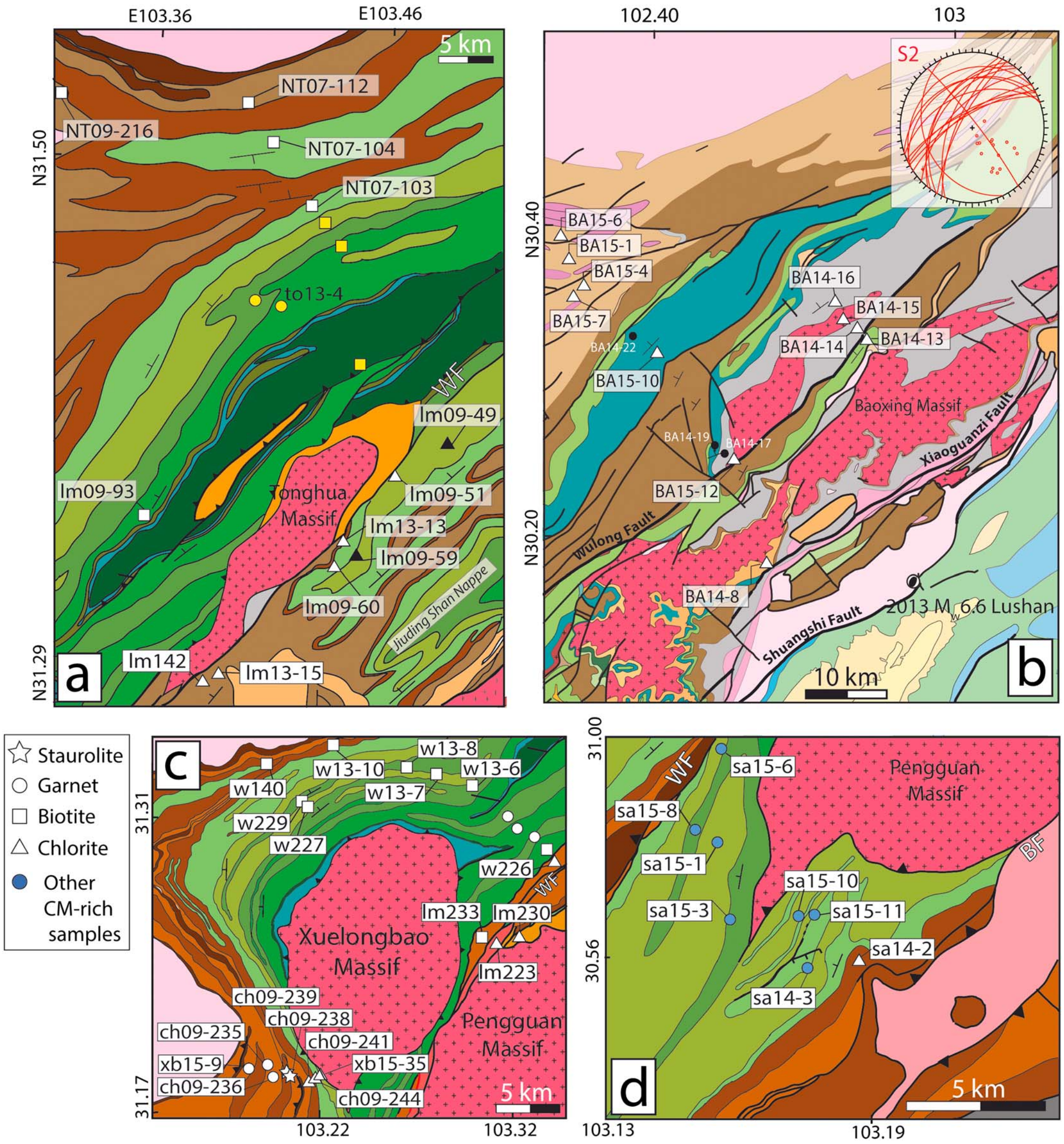

Figure 2. Enlarged views of the geological map of the studied transects. (a) Area of the Tonghua transect (samples NT) and Jiuding Shan Nappe (samples lm). Symbols in yellow indicate the mineral assemblage observed by Airaghi, Lanari, et al. (2017). Black: field stops (no sample collected). (b) Studied area in the southern Longmen Shan. The Baoxing crystalline massif (basement) crops out into two slices. The inset shows de direction and dip of S2 along the transect from samples ba14–8 to sample ba15–6. Black dots: field stops (no sample collected). (c) Location of the South Tonghua and Shapai transects in the Xuelongbao area. (d) Sanjiang transect area.

pseudotachylites of the BF (Zheng et al., 2016) suggest a compressive phase of deformation during the Late Triassic-Early Jurassic, driven by the closure of the Paleotethys. Recent petrochronological studies have also documented a metamorphic and deformation event in the central LMS at the Early Cretaceous (Airaghi, de Sigoyer, et al., 2017; Airaghi et al., 2018). These studies are however still sparse and often restricted to the higher metamorphic units of the belt, limiting our understanding of the Mesozoic thermal and structural evolution of the LMS. Furthermore, substantial differences exist between the central and southern part of the belt. Structural and geochronological data show that the southern LMS experienced thickening and deformation during the Late Cretaceous-Early Paleogene (Tian et al., 2016). The southern area exhibits higher mean elevation, lower relief, and lower channel steepness than the central LMS (H. Zhang et al., 2011). In the southern LMS the deformation propagated into the Sichuan basin, and the southern Sichuan basin was the only locus of deposition along the belt during the Cenozoic (Burchfiel et al., 1995; Densmore et al., 2007). Differences between the southern and central LMS are also observed in the present tectonics.

The 2008 M_w 7.9 Wenchuan earthquake epicenter was located on the BF, which was reactivated with a thrusting and dextral strike-slip movements (e.g., de Michele et al., 2010; X. Xu et al., 2009). The 2013 M_w 6.6 Lushan earthquake ruptured instead the Range Front Blind Thrust (RFBT), below the Shuangshi fault, with a pure thrusting movement (e.g., Liu et al., 2013), leaving in the middle an unbroken segment 50-km wide and put into question the connection between faults of the central and southern LMS.

Major questions therefore remain unresolved: (1) Did the southern and central LMS experience the same long-term geological evolution? (2) What does this imply in terms of long-term functioning of the major inherited faults?

This study uses a tectonopetrochronological approach to investigate if the long-term structuration of the LMS may help to understand the present tectonics. We present new field observations and structural data for both the central and southern LMS, a comprehensive data set of the paleotemperatures across the belt and the first barometric estimates for the low-grade metasedimentary rocks in the external domain of the central LMS (east of the WF) and in the southern LMS. This will allow us to (1) estimate the total exhumation cumulated during multiple deformation phases across the major faults, (2) discuss the link between the fault systems of the central and southern LMS at the long-term scale, and (3) unravel an asymmetry in the geological evolution of the belt since the Mesozoic. The features recognized for the LMS may be characteristic of the evolution of other intracontinental thrust belts.

2. Geological Setting and Studied Areas

In the central and southern LMS, the Neoproterozoic South China basement crops out through the sedimentary cover in the Xuelongbao, Tonghua, Pengguan, and Baoxing massifs (E. Meng et al., 2015; Yan et al., 2008; Zhou et al., 2006; Figures 1a–1c and 2). Close to the BF and within the WSZ, the crystalline massifs are affected by a brittle-ductile deformation underlined by multiples centimeter- to meter-scale greenschist facies metamorphic shear zones and veins of few millimeters to few centimeters. Metamorphic overprint occurred at 280 ± 30 °C, 7 ± 1 kbar (Pengguan massif) and 370 ± 35 °C, 7 ± 1 kbar (Tonghua massif) at ca. 140–137 Ma (Airaghi, de Sigoyer, et al., 2017; Airaghi et al., 2018). Close to the Wulong fault (WuF) the northern slice of the Baoxing massif (Figure 2b) is also strongly deformed (up to mylonitization; Tian et al., 2016; this study).

Stratigraphic and structural relations within the Paleozoic-Mesozoic metasedimentary cover allow three distinct sedimentary provinces to be recognized. They include the following:

1. *Allochtonous* units constituted by a thick (up 15 km prior to deformation; Calassou, 1994) series of strongly deformed and metamorphosed Paleozoic-Lower Triassic pelitic-dominated sediments deposited in the SPG domain (Burchfiel et al., 1995; Chen & Wilson, 1995; Robert, Pubellier, et al., 2010; Yan et al., 2011). About 40 km northwest of the WF the sediments are intruded by different generations of syn to post deformation granites emplaced between 224 and 188 Ma (de Sigoyer et al., 2014; Roger et al., 2004), at a depth of 7–11 km (Deschamps et al., 2018; Dirks et al., 1994). The metasedimentary cover of the Tonghua and Xuelongbao massifs underwent an amphibolite-facies metamorphism at 9–12 kbar, 530–580 °C (ca. 220–180 Ma) underlined by Grt + Bt + Wm ± St (abbreviations are from Whitney & Evans, 2010, except Wm = white mica) and followed by a greenschist facies overprint at 2–5 kbar, 350–400 °C at ca. 140 Ma (Airaghi, Lanari, et al., 2017, Airaghi et al., 2018; Dirks et al., 1994; Worley & Wilson, 1996);
2. *Paraautochtonous* units of SPG origin mainly cropping out southeast of the WF and northwest of the NW dipping *West Slope Fault* (WSF in Figures 1b and 1c), in the Jiuding Shan Nappe (Chen & Wilson, 1995; E. Wang et al., 2014). These units are also highly deformed and include a series of marbles, carbonates, and metapelites deposed on the South China margin in a more proximal environment compared to the allochthonous units (Burchfiel et al., 1995; Li, Yan, et al., 2014). At the southern end of the Pengguan massif and in the foreland system paraautochtonous Devonian to Triassic units crop out as a system of klippen (Chen & Wilson, 1995; Robert, Pubellier, et al., 2010; Zheng et al., 2014);
3. *Autochtonous* units (~5-km thick prior to deformation) are characterized by a carbonated-dominated stratigraphy suggestive of a platform depositional environment (e.g., Li et al., 2003). They crop out at the front of the belt with a typical structure of a fold and thrust belt and triangle zones (Jia et al., 2006; Robert, 2011). In the footwall of the BF no metamorphism is observed.

For the sake of clarity, three domains will be distinguished in the following: (1) the internal units including the terrains west of the WF in the central LMS, (2) the external units including the terrains east of the WF (the

Pengguan massifs and its sedimentary cover), and (3) the units of the southern LMS (Baoxing massif and its metasedimentary cover). In the central LMS, a series of structural measurements, observations, and samples were collected along four transects perpendicular to the major structures (*North Tonghua transect*, samples labeled NT in Figure 2a; *Shapai transect,* samples labeled XB or CH in Figure 2c; *South Tonghua transect,* samples labeled W in Figure 2c; *Sanjiang transect*, samples labeled SA Figure 2d). A fifth transect in the *southern LMS* (samples labeled BA in Figure 2b) that includes both the basement (northern slice of the Baoxing massif) and its metasedimentary cover was also studied. Samples collected along transects were supplemented by isolated samples collected in the Jiuding Nappe, in the Sinian sediments roofing the northern Pengguan crystalline massif, in the immediate footwall of the WF and in the foreland belt (samples labeled LM, Figures 1b and 2a).

3. Field Structures

3.1. The Central LMS

3.1.1. Internal Units

In a regional framework the intensity of the deformation of the Paleozoic metasedimentary series in the internal units increases from the SPG terrain eastward, approaching the WSZ, where the base of the SPG sedimentary pile is exhumed and is particularly relevant close to the contact with the crystalline massifs around which structures are deflected (Figure 3). In all metasedimentary units, macrostructures related to three phases of ductile deformation (D1, D2, D3) and a late brittle-ductile deformation phase (D4) were observed, with different degrees of preservation that vary locally. In the crystalline basement, the D3 and D4 were mainly observed.

The first (D1) is particularly preserved in the North Tonghua transect. It is characterized by a pervasive subvertical slate cleavage (S1) striking from N30-N55 in the northernmost areas to N10-N40 north of the Sanjiang area (Figures 3, 4a, and 4c).

S1 is mildly crenulated during a second deformation phase D2 according to steeply plunging upright to inclined F2 fold axes striking N60-N75 (Figure 3). F2 folds are similar, tight to isoclinal and show in general symmetrical limbs (Figures 4d and 4e). The main S2 cleavage develops parallel to the F2 axial planes (Figures 3 and 4a–4c). The S2 is deflected around the Xuelongbao massif (Figure 3). At a large scale, D2 is responsible for the folding of the internal metasedimentary units along the Tonghua transect in a NE-SW oriented and SE verging anticline and of the Silurian metasedimentary rocks along the Shapai transect in a system of tight double-verging anticlines and synclines due to the deflection of the structures around the Xuelongbao massif (Figures 2c and 3). Here subparallel E verging thrusts (N20–30 W40–80, top-to-E shearing) slice the Devonian-Carboniferous units (Figures 3 and 4g).

The third ductile deformation phase D3 is responsible for the folding of the S2 and F2, according to F3 folds axes (F3 in Figures 3, 4a, 4c, and 4d). This results in undulated F2 fold hinges or in twisted F2 folds. Folds tighten approaching the crystalline massifs. F3 are generally asymmetric, opened folds, and develop with subhorizontal axes striking at low angle with the north (Figures 3 and 4f). D3 leaded to a coplanar and oblique reactivation of the S2 cleavage resulting in C3/S2-S3 composite structures (Figure 4h). C/S structures indicate a top-to-SE sense of shear. Quartz veins associated with D2 are deformed by F3 resulting in quartz boudins (yellow in Figure 4d). D3 is particularly well expressed in the Xuelongbao transect and north of the Sanjiang area. The contact between the Xuelongbao massif and the Silurian sediments is tectonic as attested by the pervasive deformation affecting the limit between the two lithologies (with C/S structures showing a top-to-E movement).

The different populations of striae recorded at the surfaces of single fault planes in the metasedimentary rocks indicate that the majority of the faults experienced an early thrusting movement followed by one or more reactivations as normal or strike-slip faults related to the brittle deformation D4. The preserved thrust faults are generally N50-N70 (except along the Shapai transect were they are N20-N28), dipping 40–75W and show a top to southeast sense of shear (line 80–84NE). In the Devonian units east of the WF (outcrop lm142, Figure 2a) thrust faults were reactivated first as normal faults (line 56SW) and then with a dextral strike-slip movement as indicated by subhorizontal striae (9SW). In the Silurian metasedimentary rocks along the Tonghua transect (outcrop to13–4, Figure 2a), thrust faults were instead first reactivated with a dextral strike-slip movement then with a normal movement. Dextral strike-slip faults are subvertical and oriented

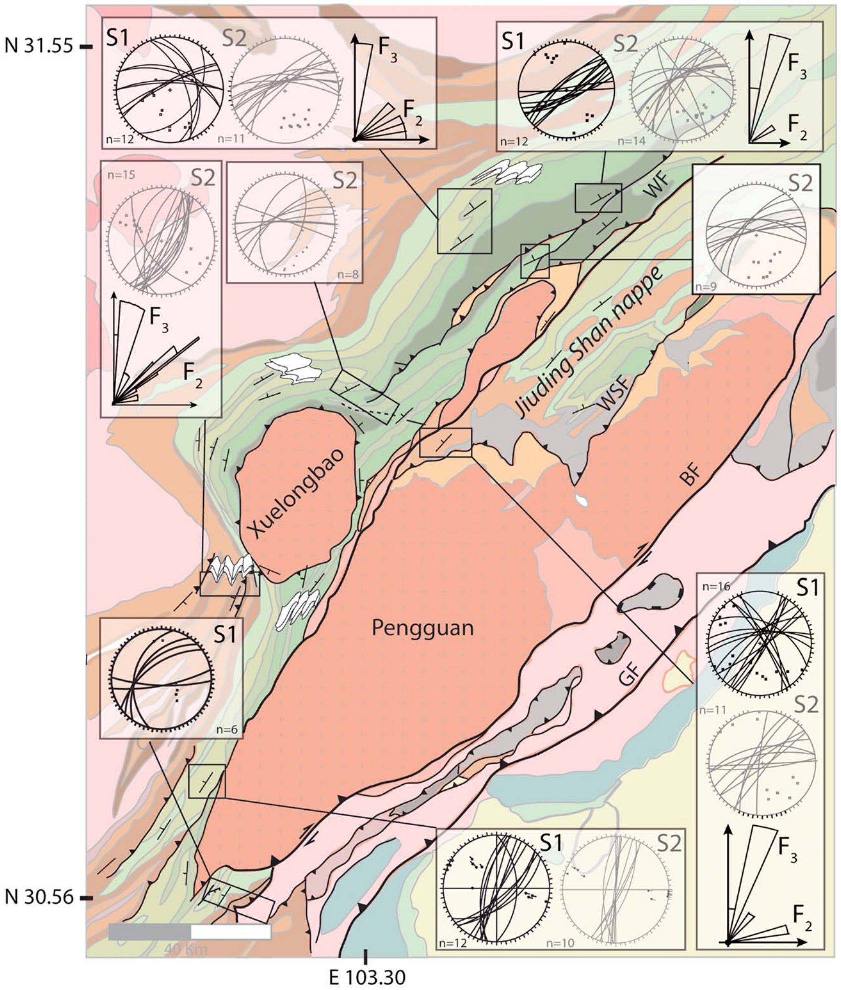

Figure 3. Structural map of the central Longmen Shan, based on our field investigations, superimposed on the geological map of the Longmen Shan and Songpan-Garze area adapted from 1:200,000 geologic map (SBGMR (Sichuan Bureau of Geology and Mineral Resources), 1991). Black and grey stereograms indicate the orientations and dips of the S1 and S2 cleavages, respectively. Rose diagrams represent the distribution of the main direction of the F2 and F3 folds measured in the field. Major tectonic discontinuities are indicated by continuous black lines. WF: Wenchuan fault, WSF: West Slope fault, BF: Beichuan fault, GF: Guanxian fault.

N50–62 (line 4E). Normal faults oriented N70, dipping 70–80W are locally observed north of the Pengguan massif and no large normal detachments were identified.

3.1.2. External Units

Three phases of ductile deformation were also observed in the external sedimentary units of the LMS. They are confined to the Silurian to Devonian paraautochthonous sediments of the Jiuding Shan Nappe. In this area the main cleavage is the S2-oriented N35, NW dipping and associated with F2 folds. F2 are folded by later F3 folds (Figure 3). In the paraautochtonous units of the Sanjiang sector, Silurian sediments are folded by F2 and F3 faults and exhibit C3-S3 structures. C planes are flatter than S, strike in average at N161 27SE and are associated with NNW SSE trending folds (Figure 3).

In the autochthonous units east of the WSF, the deformation is less intense and only one cleavage oriented N30 to N95 affects the original stratigraphy (S0) and is related to large folds. In the autochthonous units of the Sanjiang sector, east of the BF, only one ductile deformation phase is superimposed to the stratigraphy S0.

3.2. The Southern LMS

In the southern LMS, the Neoproterozoic crystalline basement crops out in two slices in the hanging walls of the Wulong and Xiaoguanzi faults (as in the internal and external domains of the central LMS). In the hanging

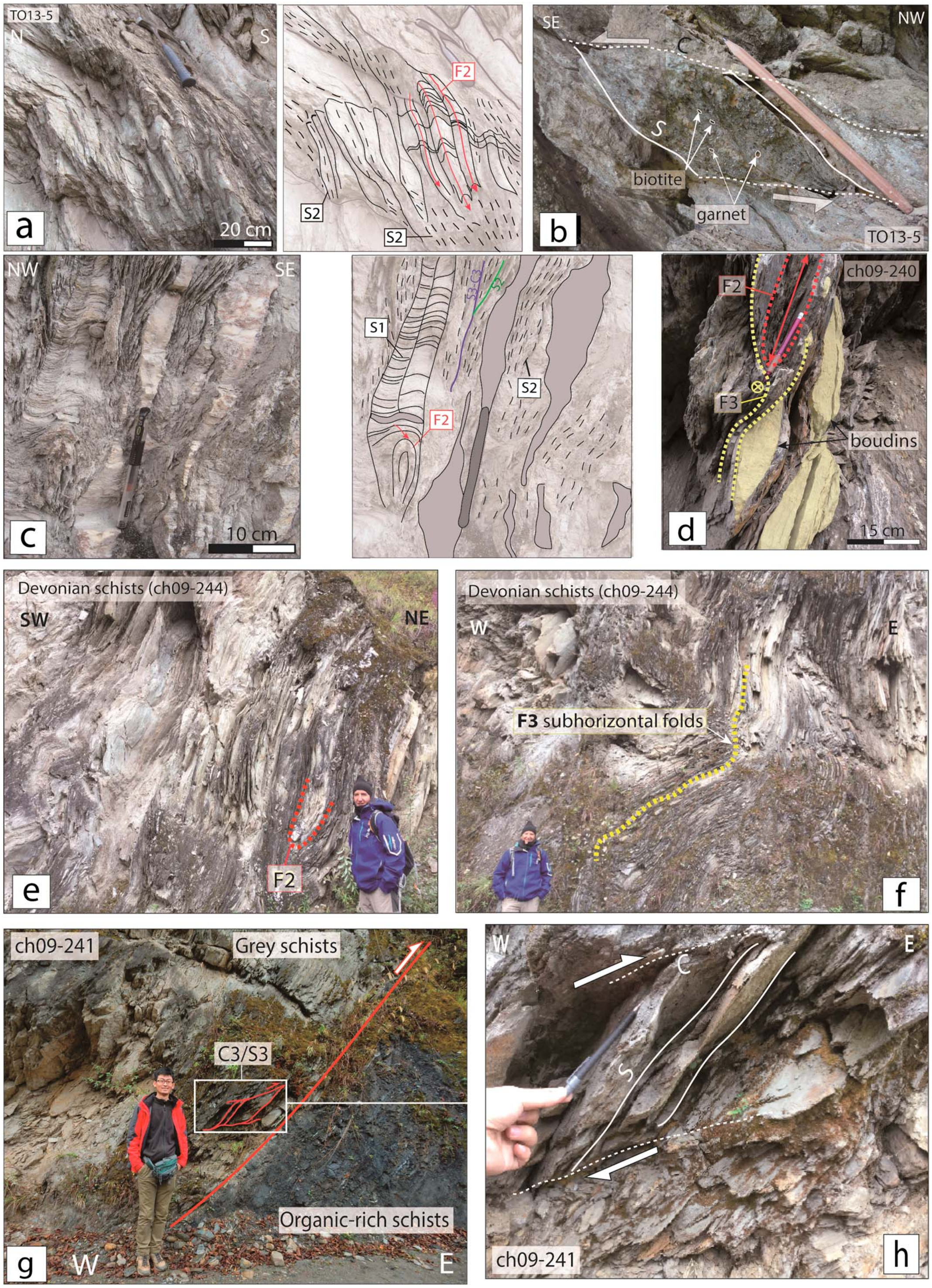

Figure 4. Photographs of the mesoscale structures observed in the field (internal units of central LMS). (a) Pervasive S2 crenulation cleavage (parallel to F2 folds) in the Silurian sediments of the North Tonghua transect. F2 axes are folded (modified from A. Robert, 2011). (b) Top-to-SE C/S structures in the garnet-biotite bearing metapelites of the North Tonghua section (close to locality to13–5 in Figure 2a). (c) S1 and S2 cleavage preserved in the Silurian sediments north of the Tonghua massif. F2 are twisted (modified from A. Robert, 2011). (d) F2 and F3 folds in the Devonian sediments of the Shapai transect. Quartz veins form bundins (yellow). (e) F2 folds in the Devonian sediments of the Shapai transect. (f) F3 folds observed close to the figure of panel e. (g) Top-to-ESE thrust slicing the Devonian metasedimentary cover in the Shapai transect. (h) C3-S3 structures showing a top-to-SE shearing in the Devonian sediments of the Shapai transect.

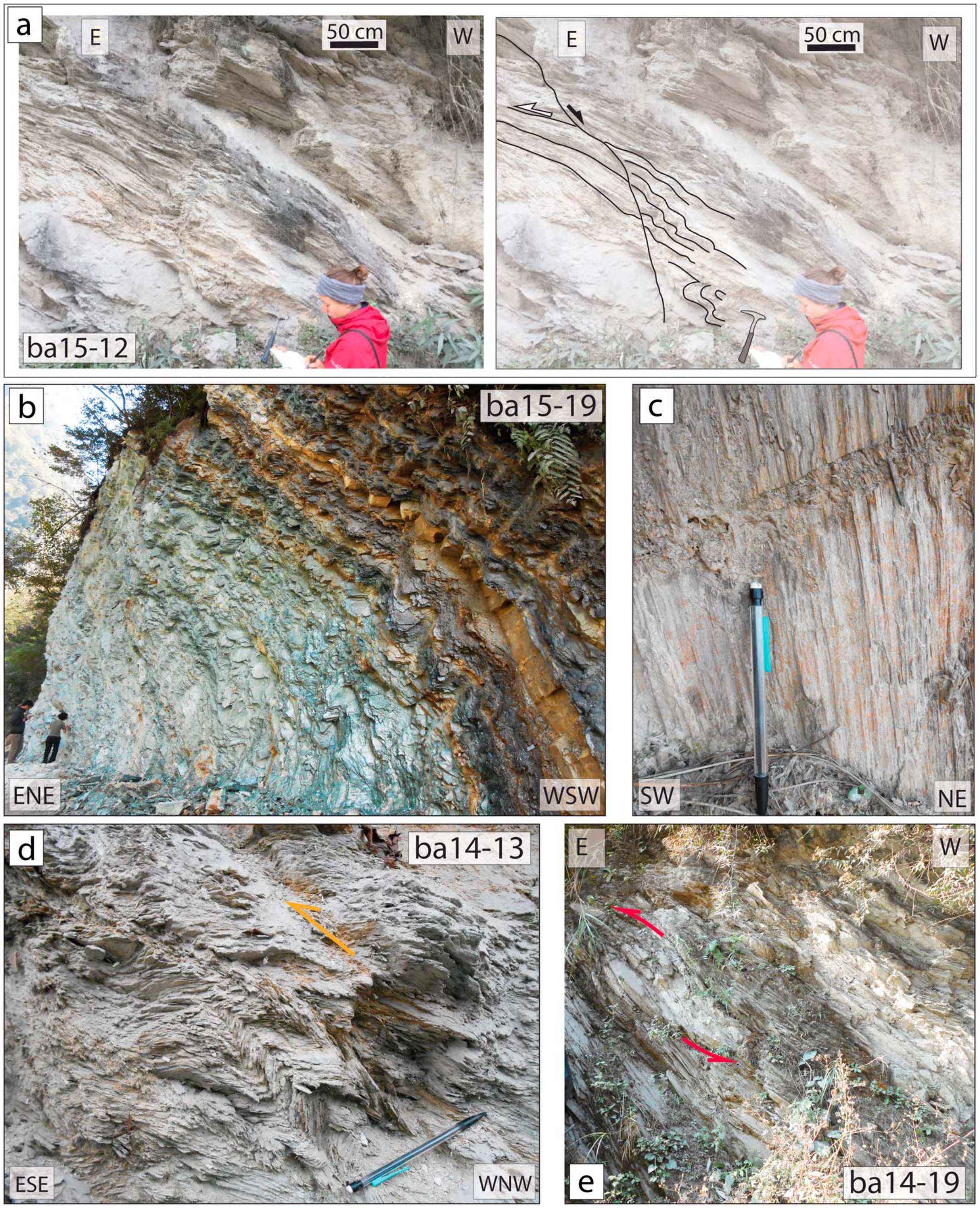

Figure 5. Photographs of the mesoscale structures in the southern LMS. (a) Top-to-E shearing structures in mylonitic zones of the basement lately cross cut by top-to-W normal faults. (b) Pervasive schistosity parallel to the bedding in the Ordovician units close to the outcrop ba14–22 (Figure 2b). (c) Constriction features in the Proterozoic units close to the outcrop ba14–17. (d) Kink bands close to the outcrop ba14–13. (e) Top-to-E shearing structures in the Silurian sediments close to the outcrop ba14–19.

wall of the Xiaoguanzi fault, the basement is weakly deformed. Metamorphic veins, a few millimeter- to centimeter-thick (filled with greenschist facies mineral assemblages) locally cross cut the magmatic foliation. The strongest deformation is observed in the immediate hanging wall of the WuF, where the basement is folded in a large-scale antiform and exhibits mylonitc and schistose zones (Figures 2b and 5a) alternating with undeformed zones. Within the most deformed rocks, C-S structures showing a top-to-E sense of shear are observed (C N22 W30, S N25 W66, stretching lineation of N98; Figures 2b and 5a). Late W dipping semibrittle normal faults (oriented N10 SW65) showing a top-to-the-W movement cross cut the earlier deformation (Figure 5a). The ductile deformation within the basement underlined by pervasive schistosity is associated with metamorphic minerals typical of the greenschist facies conditions, including white mica, chlorite, and epidote.

The metasedimetary cover of Paleozoic marbles, limestone, calc-schists, sandstones, and Triassic flysch is very deformed west of the WuF (in a structural position equivalent to the internal domain of the central LMS), forming a system of NE-SW oriented and SE verging folds (axes N18 to N56, S1–S2 N69–N41; Figure 2b). The main cleavage particularly tight in the Silurian units is west dipping, subparallel to the bedding (Figure 5b). Along the SE-NW directed transect crossing the Ordovician to Triassic sedimentary series (Figure 2b), C-S structures indicate a top-to-E sense of shear (Figure 5e) and are defined by greenschist facies metamorphic minerals including white mica and chlorite developing in metamorphic veins or pervasively in larger volumes of rock. Three kilometers west of the WuF (hanging wall), gauge zones made by metric blocs within a thin matrix are observed in the Proterozoic metasedimentary rocks (ba14-14 in Figure 2b). Here rocks are deformed (ba14-17) with the streaching lineation strongly dominant over the schistosity (S N65 66NW, pitch of L 78NW, Figure 5c).

In the immediate footwall of the WuF (ba14–13 in Figure 2b), Silurian rocks are folded to form kink bands (Figure 5d), suggesting a brittle-ductile deformation. Eastward-plunging structures were locally observed; they were interpreted as the result of the tilting of original structures during the Cenozoic re-activation of the belt. No medium-grade metamorphic minerals were observed in the southern LMS as it was instead the case in the central part of the belt.

4. Sampling and Sample Description

Fifty-seven samples were collected for this study. Their elevations range between 1,585 and 1,710 m (North Tonghua), between 1,460 and 1,545 m (South Tonghua), between 2,047 and 1,850 m (Shapai), between 1,720 and 1,810 m (Sanjiang), and between 1,100 and 1,300 m in the southern LMS (Baoxing area).

Among collected samples, 49 were organic-rich schists and carbonates suitable for the Raman Spectroscopy on Carbonaceous Material (RSCM) thermometry (Table S1 in the supporting information). The mineralogy of samples from the North and South Tonghua transects is described in details elsewhere (Airaghi, Lanari, et al., 2017; Airaghi et al., 2018).

4.1. Central LMS

4.1.1. Internal Units (Shapai Transect)

Samples from the Shapai transect collected for thermometric purposes (see Figure 2c) exhibit three types of ductile microstructures related to three ductile deformation phases (D1, D2, D3). An early cleavage S1 (D1) is preserved in the inclusion trails of Grt, Bt, and St porphyroblasts (Figures 6a and 6b). S1 is folded by a white-mica bearing crenulation cleavage S2 (D2; Figures 6a–6c). Euhedral porphyroblasts of Bt (±Grt, ±St) 500 μm–3 mm in size are rotated and wrapped in the S2 cleavage (Figures 6a and 6b) and exhibit crenulated surfaces (Figure 6b). Staurolite is only observed in samples collected in a narrow zone along the Shapai transect as 500 μm up to 3 cm porphyroblasts with X-shaped twins (Figure 6b). No kyanite was observed. Biotite and ilmenite developed in pressure shadows around staurolite. Samples close to the Xuelongbao massif (e.g., ch09-241 and ch09-244) exhibit a tight folded cleavage made of elongated crystals of white mica and quartz microlithons (Figure 6c) and no high-grade metamorphic minerals. White mica is folded at both the micrometric and the centimeter-scale along with Qz veins, while in the less deformed domains relicts of biotite are preserved. Chlorite appears as crenulated flakes 200–500 μm large (Figure 6c).

Approaching the WSZ, only greenschist facies metamorphic assemblages are observed. In the strongly deformed sample lm223 (Long. 103.6049, Lat. 31.3885), collected within the WSZ, eye-shaped nodules composed of Qz, brown to yellow Ep 200–300 μm in length, and Chl replacing Grt are wrapped in the main cleavage (Figure 6d).

4.1.2. External Units

In rocks of the external domain of the LMS, the only metamorphic assemblage characteristic of the greenschist facies conditions was observed made of Qz + K-Wm + Chl + Ep + Fs + oxides. In the paraautochtonous units of the Jiuding Shan Nappe (e.g., organic-rich schist lm09-59, Long. 103.7448, Lat. 31.5734), the S1 cleavage is subparallel to S0 (white layer in Figure 6e) and crosscut by discrete S2

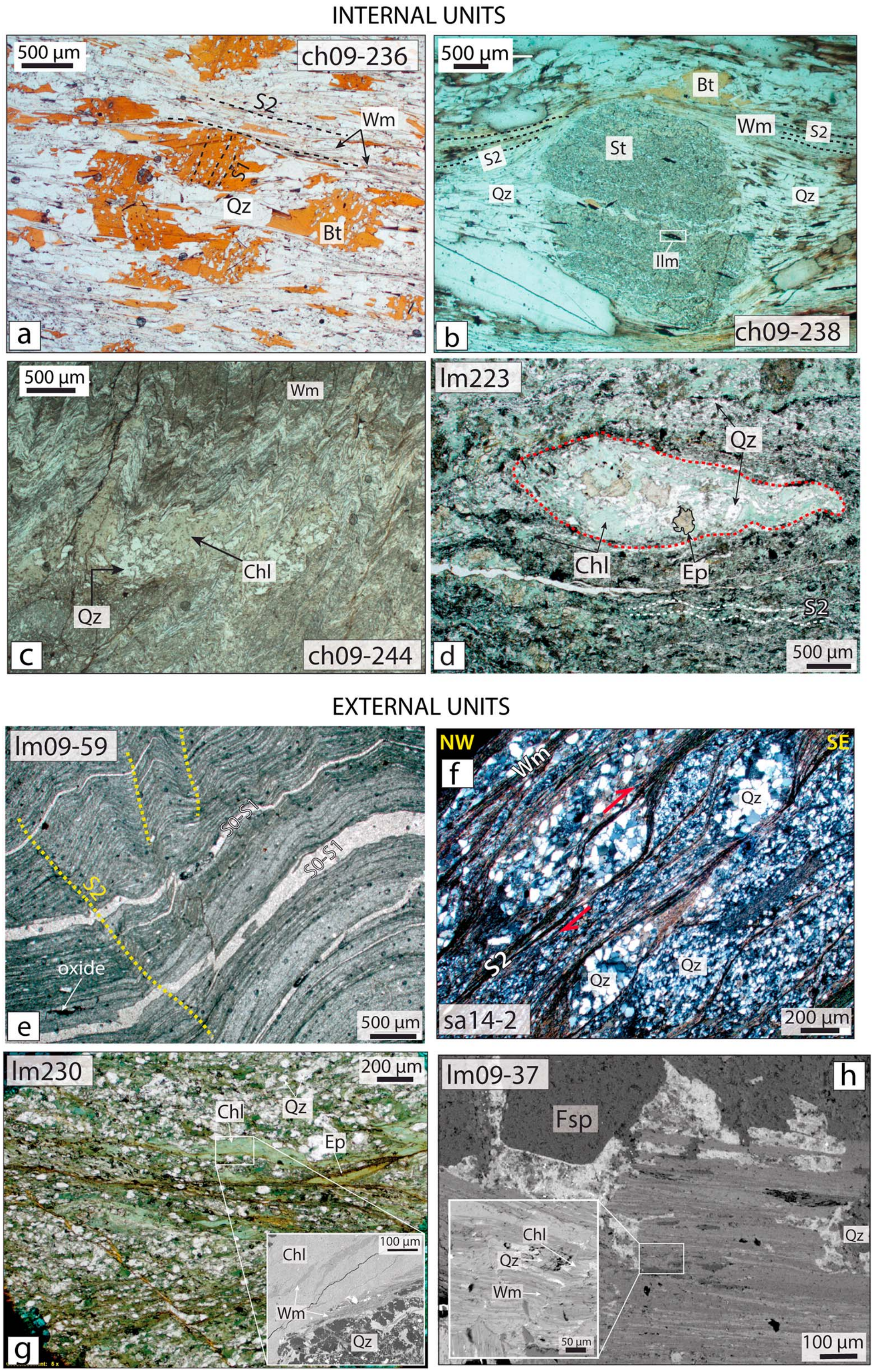

Figure 6. Photomicrographs of representative samples collected in the internal and external metasedimentary units. Abbreviation are from Whitney and Evans (2010), except Wm = white mica. (a) Biotite-bearing schistosity along the Shapai transect. (b) Deformed staurolite porphyroblast in the Shapai area. (c) Chl-Wm microfolds close to the contact between the metasedimentary cover and the Xuelongbao massif. (d) Ep + Qz + Chl pseudomorph of garnet close to the WSZ. (e) Greenschist facies bearing assemblage in sample lm230. (f) Deformed organic-rich schist lm09–59. (g) Backscatter image (BSE) of the Chl + Wm intergrowths in sample lm09–37. (h) Plain Polarized Light (PPL) image of the Wm-bearing metagreywacke sa14–2.

crenulation cleavage domains, folded at its turn. Oxides constitute aggregates with irregular borders, oriented in the main foliation, while the organic-rich material is localized in the microfolds hinges or in lenticular layers (e.g., Figure 6e).

In the Devonian paraautochtonous sedimentary units of the Sanjiang sector (e.g., sample sa14-2) only one crenulation cleavage is observed superimposed to the S0. The main cleavage is underlined by elongated grains of 50–100 μm of white mica, organic-rich material and quartz grains affected by bulging recrystallization. This cleavage wraps nodules of rounded quartz grains (of 50–100 μm) which define eye-shaped structures sheared with a top-to-ESE sense of shear (Figure 6f). No chlorite was observed in this sample.

In the Sinian sediments roofing the Pengguan massif (samples lm230 and lm09-37), rocks are the less deformed, metamorphosed under greenschist facies conditions with chlorite developing along the main cleavage and in fractures of few microns in size in association with epidote and white mica (Figure 6g). In sample lm09-37 Chl + Wm intergrowths develop in large (500–800 μm) flakes among Qz, Fs (±Ap; Figure 6h).

4.2. The Southern LMS

Among samples collected in the southern LMS for thermobarometric purposes, ba14-15 and ba15-12 belong to the crystalline basement. Sample ba14-15 is a deformed metagranite where the magmatic assemblage of Fs + Pl + Qz + Bt is overprinted by secondary white mica stretched in zones of high strain (Figure 7a). Feldspar is partly sericitized and quartz recrystallizes by bulging. The metagranite ba15-12 is mylonitic, with assemblage of Wm + Fs (K-fs and Ab) + Qz ± Pl ± Bt ± Ap. Two samples were collected from this outcrop. One (ba15-12c) exhibits C-S structures; the foliation (S) is defined by elongated chlorite and tiny white mica-rich layers, while shear planes (C) are defined by epidote (Figure 7b). Feldspar is sericitized and locally defines eyes wrapped in the foliation. Feldspar and plagioclase show intracrystalline deformation features, including deformation twins, patchy ondulose extinction, and subgrains with weakly defined boundaries. Large quartz grains exhibit an ondulose extinction, subgrains parallel to microcracks and irregular grain boundaries due to grain boundary migration (Figure 7c). Around larger grains, small grains form by bulging. The other sample of the same outcrop, ba15-12d, shows a pervasive foliation made of submillimeter quartz grains and white mica layers wrapping the weakly sericitized and deformed feldspar eye-shaped grains and defining a top-to-E shearing (Figure 7d). Quartz recrystallizes by subgrain rotation in the matrix and by bulging around feldspar.

Among samples collected in the metasedimentary cover, ba15-1f represents a typical organic material-rich sample, with an early S0-S1 cleavage deformed by a later S2 (Figure 7e). Sample ba15-10 is a deformed black schist with pelitic layers hosting greenschist facies mineral assemblages. A pervasive foliation (S0-S1) is cross cut by quartz veins rimmed by Chl + Wm + Qz (Figure 7f). Larger quartz grains exhibit folded inclusion trails and subgrains. Quartz recrystallized into smaller grains by bulging and subgrain rotation. Sample ba14-14 is a Ca-rich metagraywacke with allochtonous grains of quartz and calcite wrapped in the main foliation formed by white mica layers and polycrystalline aggregates of quartz developed by subgrain rotation recrystallization (Figure 7g). Microstructures show a top-to-E shearing (Figure 7g). The top-to-E shearing is therefore associated with greenschist facies conditions.

5. Analytical and Computational Methods

The chemical compositions of the metamorphic minerals (chlorite and white mica) was analyzed to retrieve *P-T* conditions of the greenschist facies metamorphism in the external units of the central LMS and in the southern LMS. The chemical composition of metamorphic minerals related to the amphibolite facies metamorphism has been described in detail elsewhere (Airaghi, Lanari, et al., 2017; Dirks et al., 1994; Worley & Wilson, 1996) and is beyond the scope of this study.

Analyses of chlorite and white mica in samples lm230, lm09-37, sa14-2 (central LMS), and ba14-14, ba15-12, and ba15-10 (southern LMS) were acquired with a JEOL JXA-8230 electron probe microanalyzer at Institut des Science de la Terre (ISTerre, Grenoble). Accelerating voltage was fixed at 15 keV with beam current of 12 nA and beam size of 1 μm. X-ray maps in samples ba15-12d were acquired at 15 keV, 100 nA, with a dwell time of 200 ms. Maps were quantified using the program XMapTools 2.3.1 (Lanari et al., 2014).

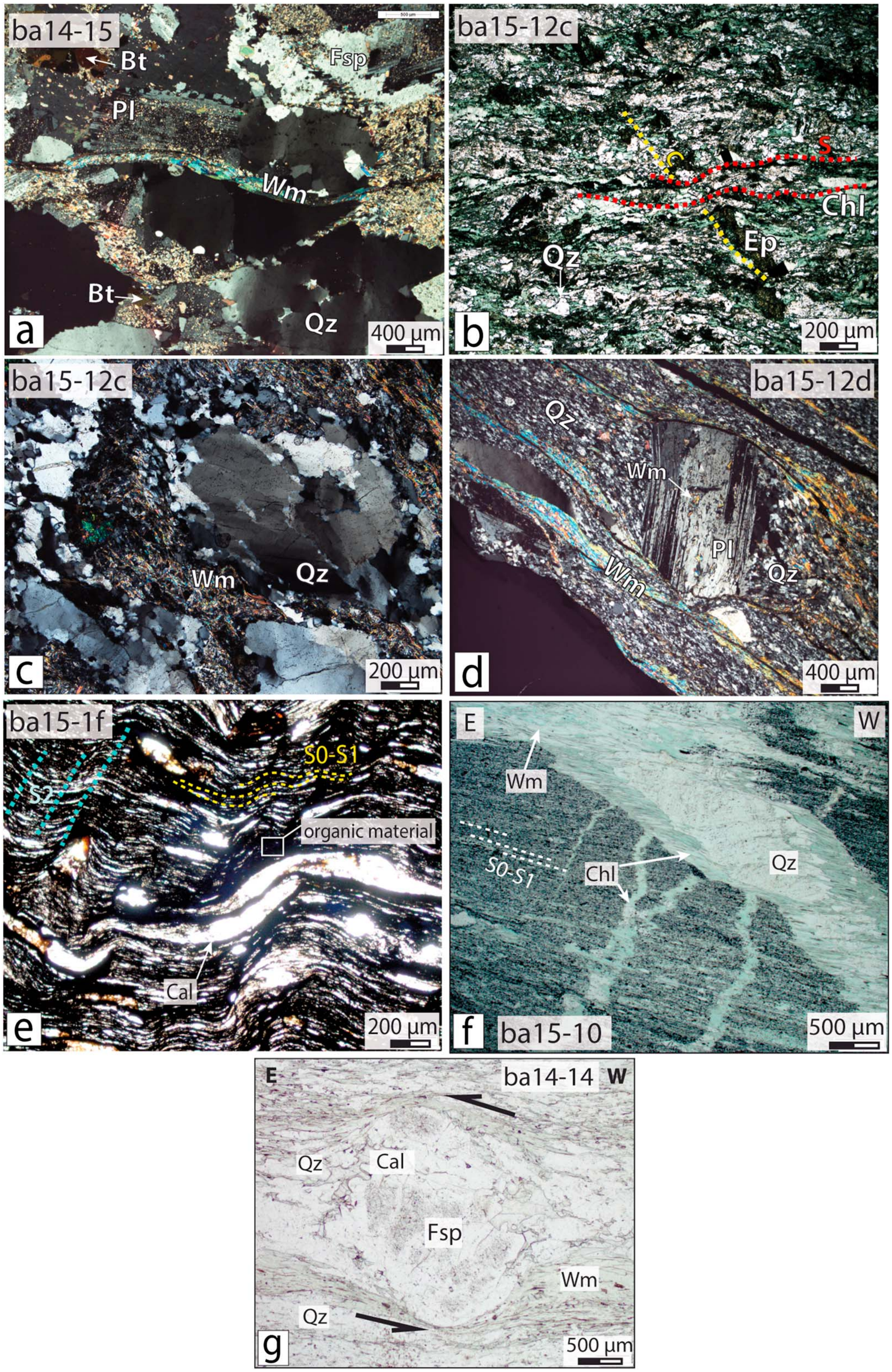

Figure 7. Photomicrographs of samples collected in the southern LMS. (a) Plain Polarized Light (PPL) image of white mica layers in metagranite ba14–15. (b) C-S structures in sample ba15–12 from the crystalline basement. (c) PPL image of quartz subgrains and recrystallization by bulging in sample ba15–12c. (d) PPL image of feldspar grains wrapped in the white mica-bearing S2 cleavage defining the main foliation. (e) Organic material-rich sample showing a S1 and S2 cleavage. (f) Chlorite and white mica assemblage in the black schist ba15–10. (g) White mica-bearing cleavage wrapping an allochthonous feldspar grain in sample ba14–14.

RSCM thermometer (Beyssac et al., 2002) was used to estimate the maximum temperature (T_{max}) experienced by the organic material-rich samples in order to provide an image of the paleotemperature at the scale of the belt. Ten to 15 spectra were acquired per sample using a Renishaw InVia Reflex microspectrometer (Paris, ENS) with a 514-nm Spectra Physics diode laser in circular polarization and processed them with the software Peakfit.

RSCM was combined with the multiequilibrium thermobarometry based on the thermodynamic properties and solid solutions models of Vidal et al. (2005, 2006) and Dubacq et al. (2010) to model the *P*-*T* conditions of the high variance assemblages involving Chl + Wm + Qz + H_2O in the samples lm230, lm09-37, sa14-14, ba15-12, and ba14-14, following the procedure described by Airaghi, de Sigoyer, et al. (2017) and Lanari et al. (2012). Metamorphic conditions were estimated from the intersection between the *P*-*T* equilibrium curves calculated for white mica and (1) the *T* calculated for Chl in textural equilibrium (lm09-37 and lm230), or (2) the *T* estimated for Chl with the thermometer of Massonne and Schreyer (1987; sample ba15-10) or the (3) T_{max} estimated with the RSCM (sa14-2) under the hypothesis that metamorphic white mica reequilibrated at the temperature peak. The same approach was used to evaluate *P* conditions of white mica growth from published chemical compositions of white mica collected in the mylonitic basement of the southern LMS by Tian et al. (2016; samples BX118 and BX127). When chlorite was not observed in the assemblage, reference temperature was fixed at 350-400 °C, based on Qz and Fsp deformation textures.

Two samples (ba14-14 and ba14-15) from the southern LMS were selected for in situ $^{40}Ar/^{39}Ar$ dating on white mica to constrain the timing of the greenschist facies metamorphism. The age of metamorphism in the central LMS has already been constrained (Airaghi, de Sigoyer, et al., 2017, Airaghi et al., 2018). The in situ $^{40}Ar/^{39}Ar$ dating was done by UV laser ablation on polished 300-μm-thick sections cut mirror-like from the ones used for petrological observations. Samples were dated at the Open University, UK, following the procedure described by Airaghi et al. (2018) and detailed in the supporting information. The fact that chemical heterogeneities in white mica may be smaller than the laser spot was taken into account and discussed below. Age uncertainties on the isotopic measurements are reported to 1σ. Only analyses showing no contamination by calcite or chlorine-bearing phases (checked with $^{38}Ar/^{39}Ar$ and $^{37}Ar/^{39}Ar$, see Table S1) were considered.

6. *P-T-t* Results

6.1. Chemical Composition of Metamorphic Minerals

Representative chemical analyses of metamorphic minerals are reported in Table 1 and Figure 8. In samples lm09-37, lm230 and sa14-2 from the central LMS, the white mica exhibits a homogeneous chemical composition. Among them, white mica in sa14-2 is the one that exhibits the lowest Si^{4+} content and X_{Mg}. In the crystalline basement of the southern LMS (sample ba15-12), compositional maps reveal the existence of two chemical groups of white mica (dominant muscovite composition of 50–70%, Figure 8a) occupying different microstructural sites. A Ti-rich, Fe-rich white mica is observed in the core of the white mica-bearing layers, along microcracks crossing the relicts of ilmenite. This group (Wm1) shows the highest Si^{4+}, Ti^{4+} contents and the lowest X_{Mg} (Figure 8a and Table 1). Si^{4+} progressively decreases from the core to the rim of the white mica-bearing layer (Figure 8a). The second compositional group of white mica (Wm2), with lower Si^{4+}, Ti^{4+} contents wraps the Wm1 grains and forms the rims of the white-mica-rich layers. In sample ba15-10 and ba14-14 (metasedimentary cover) white mica and chlorite exhibit a homogeneous chemical composition within each sample (Table 1), with white mica in sample ba14-14 exhibiting higher Si^{4+} and lower X_{Mg} than white mica in sample ba15-10 (Figure 8a). Chlorite also exhibits a homogeneous composition within each sample (Figure 8b). The lowest Si^{4+} and highest X_{Mg} is measured in chlorite of sample ba14-14 (Figure 8b).

6.2. Thermobarometric and Geochronological Results

The 49 new maximum temperatures obtained by RSCM are summarized Table S1 and integrated to existing temperatures in Figures 9a and 9b. Three NW-SE oriented profiles perpendicular to the WF and BF were realized in the central LMS (were the density of samples was the highest) in order to track the temperature differences across the major structures. Samples collected in the Jiuding Nappe were projected along the profile of the North Tonghua transect (profile 2 in Figure 9a) and integrated to data from Airaghi, Lanari, et al.

Table 1
Representative Chemical Compositions of Analyzed Metamorphic Minerals (Chlorite and White Mica)

Sample	LM230		SA14-2	LM09-37		BA15-10	BA15-12c		BA14-14
Longitude	E 103.53		E 103.27	E 104.09		E 102.68	E 102.76		E 102.89
Latitude	N 31.41		N 30.97	N 31.60		N 30.53	N 30.41		N 30.56
	Wm	Chl	Wm	Wm	Chl	Chl	Wm1	Wm2	Wm
Mineral									
SiO2	47.97	28.06	47.47	49.64	28.40	27.82	48.35	46.34	46.70
TiO2	0.32	0.04	0.17	0.40	0.32	0.02	0.80	0.30	0.58
Al2O3	28.36	17.47	32.82	25.88	18.36	23.52	26.29	30.62	27.93
FeO	5.33	25.21	1.84	5.22	26.55	16.40	5.22	4.49	7.34
Fe2O3	0.00	0.00	0.00	0.00	0.00	0.00	0.00	0.00	0.00
MnO	0.00	0.47	0.00	0.03	0.56	0.10	0.03	0.02	0.03
MgO	2.89	16.45	1.43	2.95	14.30	20.18	2.10	1.49	1.10
CaO	0.00	0.09	0.03	0.16	0.06	0.01	0.01	0.01	0.00
Na2O	0.09	0.03	0.12	0.08	0.01	0.02	0.11	0.08	0.17
K2O	8.80	0.36	10.29	9.47	0.25	0.02	10.77	11.31	10.63
Total	93.76	88.19	94.16	93.83	88.82	88.09	93.68	96.66	94.48
Cations									
Si	3.28	2.94	3.19	3.30	2.97	2.76	3.35	3.17	3.24
Ti	0.02	0.00	0.01	0.01	0.03	0.00	0.04	0.02	0.03
Al	2.28	2.16	2.60	2.14	2.26	2.75	2.15	2.47	2.29
Fe	0.30	2.21	0.10	0.42	2.32	1.36	0.30	0.26	0.43
Fe3	0.00	0.00	0.00	0.00	0.00	0.00	0.00	0.00	0.00
Mn	0.00	0.04	0.00	0.01	0.05	0.01	0.00	0.00	0.00
Mg	0.29	2.57	0.14	0.42	2.23	2.98	0.22	0.15	0.11
Ca	0.00	0.01	0.00	0.01	0.01	0.00	0.00	0.00	0.00
Na	0.01	0.01	0.02	0.01	0.00	0.00	0.01	0.01	0.02
K	0.77	0.05	0.88	0.64	0.03	0.00	0.95	0.99	0.94
Oxygens	11	14	11	11	14	14	11	11	11
XMg	0.49	0.54	0.58	0.50	0.49	0.69	0.42	0.37	0.21

(2017). Samples of the Sanjiang sector were integrated to temperatures obtained by Robert, Pubellier, et al. (2010) in the Gengda area (Figure 9a and profile 3 in Figure 9a).

In the hanging wall of the WSZ T_{max} range between 502 and 619 °C (±30 °C) with few localities showing T_{max} between 470 and 481 °C. Samples that experienced the highest T_{max} of 594–619 °C are located in the Devonian series along the Shapai transect. In all profiles of the hanging wall of the WF, isotherms define peaks, with systematic temperature variations of 30–50 °C (above the thermometer uncertainty), drawing a series of antiforms and synforms progressively tightened approaching the WF (e.g., profile 3 in Figure 9a). Close to the WF, samples show $T_{max} > 500$ °C despite a mineral assemblage typical of the greenschist facies conditions. Along all transects, T_{max} sharply decrease to ~150 °C across the WSZ: it does not exceed 380 °C (±30 °C) in its footwall. The temperature jump is sharp and restrained to a band few meters to few kilometers wide. A thermal jump of ~50 °C is also observed across the BF, where T_{max} decrease from 350–380 °C (hanging wall) to <330 °C in the foreland belt (Figure 9a). In the metasedimentary cover of the southern LMS T_{max} do not exceed 394 °C ± 30 °C and no major temperature jumps are observed across the faults along the studied transect (Figure 9b and Table S1).

P-T equilibrium conditions for sample lm09-37 and lm230 yield at 300 ± 30 °C, 8 ± 1 kbar and 300 ± 30 °C, 7 ± 1.5 kbar, respectively (Figure 10a), while sample sa14-2 shows a lower pressure of 4.5 ± 2 kbar for RSCM temperatures of 340 ± 30 °C (Figure 10b). In the Baoxing crystalline basement (sample ba15-12) *P-T* conditions yield at 360 ± 30 °C, 6 ± 2 kbar. Wm1 plot at slightly higher pressure than Wm2 for the same temperature range (Figure 10c). *P-T* estimates for white mica analyses from Tian et al. (2016) provide consistent *P-T* results (Figure 10d) at 6.5 ± 3 kbar, with the highest density of analyses at 6 ± 1 kbar, 350–400 °C. The *P*-map obtained with the barometer of Massonne and Schreyer (1987) shows *P* conditions of 7–7.5 kbar for Wm1 and of 5.5 kbar for Wm2, with intermediate values for white mica located in the

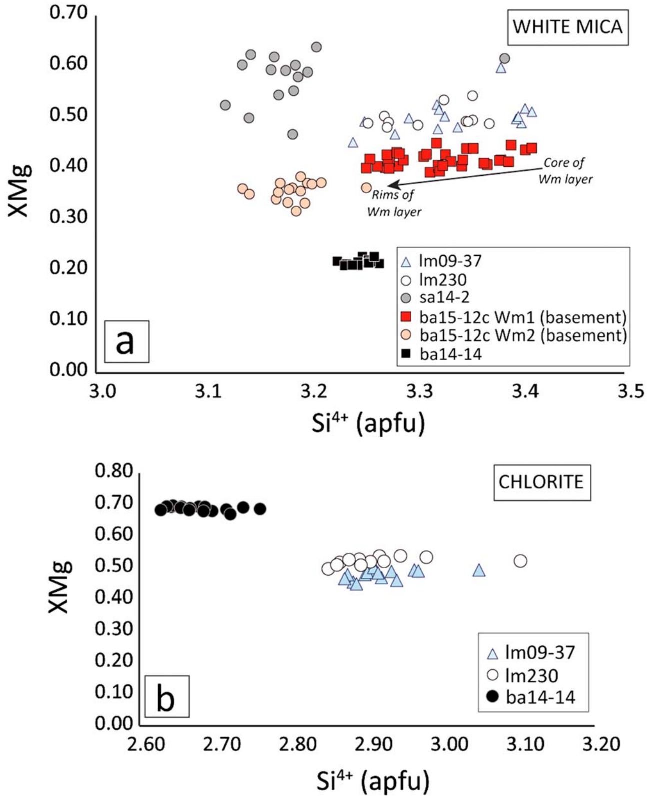

Figure 8. Si^{4+} versus X_{Mg} diagram of white mica (a) and chlorite (b) chemical compositions analyzed in samples collected for thermobarometric proposes (see text for details). The Si^{4+} of white mica 1 (Wm1) in sample ba15–12c progressively decreases from the core to the rim of the white mica-bearing layers to reach the composition of Wm2 (black arrow).

middle of the Wm-bearing layer (at $T = 400$ °C, Figure 10e). In the sedimentary cover (samples ba15-10) T conditions for chlorite yield at 350 ± 20 °C. In this temperature range, P conditions for the Wm-bearing assemblage in sample ba14-14 can be estimated at 3 ± 1 kbar, 350 ± 20 °C (Figure 10f).

Geochronological results for samples ba15-12 and ba14-14 are reported in the insets of Figures 10c and 10f and in Table S2. White mica in sample ba14-15 (basement) yielded ages between 74.6 ± 6.1 and 58.8 ± 5.7 Ma. White mica in metasedimentary sample ba14-14 yielded younger ages ranging from 52 ± 2 to 33 ± 1.3 Ma.

6.3. Interpretation of *P-T-t* Results

The range of the new RSCM T_{max} obtained for the internal units of the central LMS (>500 °C) is in line with the amphibolite facies metamorphic minerals (St, Grt) observed in the peak mineral assemblage, with temperatures reported by Robert, Pubellier, et al. (2010) and Airaghi, Lanari, et al. (2017) and with the peak metamorphic conditions estimated in Silurian and Devonian units along the South Tonghua, North Tonghua, Shapai and Gengda areas (north of the Sanjiang transects) with conventional barometry and thermodynamic modeling (Airaghi, Lanari, et al., 2017; de Sigoyer et al., 2011; Robert, 2011; Worley & Wilson, 1996). No kyanite was observed in the metasedimentary cover around the Xuelongbao massif, in contrast to the observations of Worley and Wilson (1996). The P T conditions obtained with the multiequilibrium approach for the metasedimentary cover in the external units of the central LMS are consistent with the observed greenschist facies peak mineral assemblage and are in line with temperatures obtained by RSCM.

In the southern LMS, P-T conditions are also consistent with RSCM T_{max} and the observed greenschist facies mineral assemblage. Temperature estimates in the basement are compatible with the temperature range of ~300–400 °C suggested by the ductile deformation of quartz and quartz recrystallization mainly by bulging or subgrain rotation (Passchier & Trouw, 2005; Stipp et al., 2002). The chemistry of white mica in sample ba15-12 is very similar to the one measured by Tian et al. (2016). The Ti-enrichment of the Wm1 might be due to its being grown from a Ti-rich biotite. Pressure conditions obtained for Wm1 with the Phg-Qz-H_2O modeling approach are generally close to pressure conditions obtained for Wm2, although multiple analyses of Wm2 plot at lower pressure values. In contrast, the P map obtained with the barometer of Massonne and Schreyer (1987) shows higher pressures for Wm1 (~7.5 kbar) than for Wm2 (~4 kbar). These observations may suggest decompression (exhumation) during the greenschist facies overprint and the associated deformation in the crystalline basement.

The T estimates in both the basement and in the sedimentary cover of the southern LMS are lower than the nominal closure T for Ar in muscovite (425 °C for a 100 μm radius grain, a cooling rate of 10 °C and P = 10 kbar; Harrison et al., 2009): $^{40}Ar/^{39}Ar$ dates are therefore interpreted as representing white mica crystallization ages. Since the chemical heterogeneities within white mica (10–20 μm) are smaller than the spatial resolution of the laser used for the in situ dating (~65 μm), the calculated $^{40}Ar/^{39}Ar$ age might be affected by processes other than local in situ K-Ar decay (e.g., Airaghi et al., 2018). In the Baoxing basement, the oldest ages (68–74.5 ± 6.1 Ma) could correspond to the relicts of Wm1 and the youngest ages (58–60 ± 9 Ma) to the growth of Wm2, although the influence of the white mica grain size and deformation on the age dispersion cannot be discarded. These age intervals are consistent with the white $^{40}Ar/^{39}Ar$ white mica and biotite ages obtained by Tian et al. (2016) in the basement of the southern LMS.

In the metasedimentary rocks (ba14-14), the white mica ages are younger (<55 Ma) than those in the basement. Although further investigations would be required to precisely assess the timing of the tectonometamorphic evolution of the sedimentary cover, our results clearly show that the greenschist facies metamorphism in the southern LMS is Late Cretaceous-Cenozoic in age.

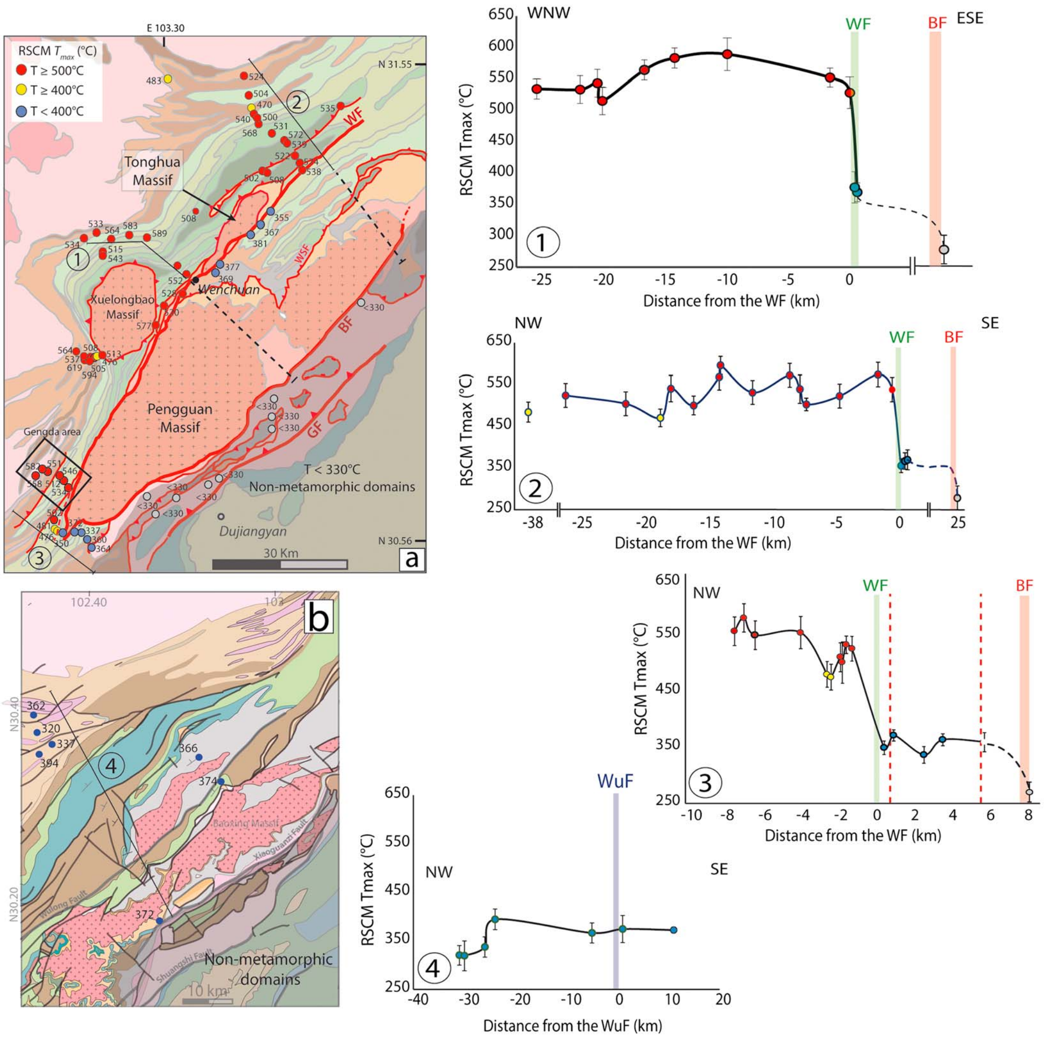

Figure 9. Maximum temperatures (T_{max}) obtained with the RSCM thermometry. (a) Distribution of T_{max} in the geological map of central (a) and southern (b) Longmen Shan. Black lines 1, 2, 3, and 4 indicate profiles on the right-hand side. WF: Wenchuan fault, BF: Beichuan fault, WuF: Wulong fault. In the profiles, the T_{max} plotted in a temperature versus distance to the WF (1, 2, 3) or WuF (4). The uncertainty reported on T_{max} is the standard deviation. Results from the Gengda area (black frame along profile 3) are from Robert, Pubellier, et al. (2010). The profile between samples in the hanging and footwall of the Beichuan fault is extrapolated (dashed black line). Dashed red lines in profile 3 represent the location of the different branches of the WF and BF.

7. Discussion

7.1. Structural and *P-T-t* Evolution of the Central LMS

A very constant deformation scheme is observed in the internal metasedimentary series of the central LMS, at different spatial scales. It includes D1, D2, D3 ductile deformation phases, and a D4 brittle-ductile phase of tilting, in line with the deformation phases observed by Harrowfield and Wilson (2005) in the Danba area and in the southern LMS. At a first-order level, therefore, the internal metasedimentary units experienced a similar deformation history. Folds tighten approaching the crystalline massifs, suggesting that the Xuelongbao, Pengguan, and Tonghua massif acted as rigid buttresses during the D2 deformation phase, although they were not yet exhumed. D2 is only observed in the metasedimentary cover and is coeval with, or postdated, the peak *T* as suggested by the folded shape of the isotherms obtained by RSCM along the transects in the internal units and the fact that magmatic intrusion in the SPG are either deformed or crosscut earlier structures (Figure 9a). In all studied transects, similar peak metamorphic mineral assemblages are associated with similar microstructures, suggesting that the metamorphic peak (9–12 kbar, 530–580 °C, Airaghi, Lanari, et al., 2017, Airaghi et al., 2018) occurred coevally in the entire internal metasedimentary units, at

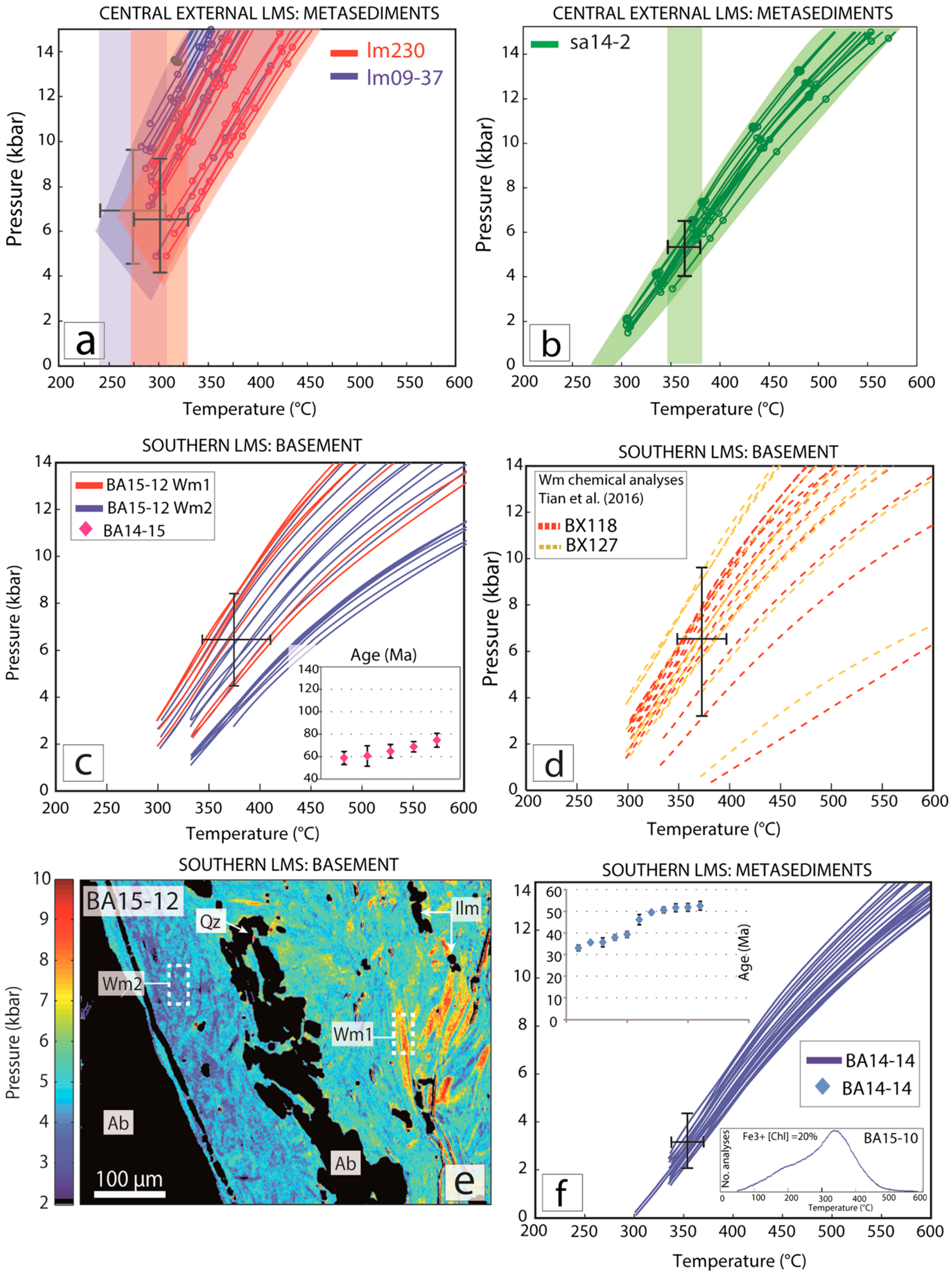

Figure 10. *P-T-t* results. (a) *P-T* white mica lines for samples lm09–37 and lm230 (sediments roofing the Pengguan massif). Colored frames are temperatures obtained from chlorite. Crosses indicate the estimated *P-T* conditions for the greenschist facies assemblage. (b) *P-T* conditions for sample sa14–2. (c) White mica *P-T* lines for samples from the basement ba15–12 in the southern Longmen Shan. Wm1 plot at slightly higher *P* (or lower *T*) than Wm2. The inset shows the ^{40}Ar/^{39}Ar white mica ages for sample ba14–15 sorted by increasing age. (c) *P-T* lines obtained from the chemical compositions of white mica analyzed by Tian et al. (2016) for samples similar to ba15–12. (e) *P*-map obtained with the barometer of Massonne and Schreyer (1987) for a white mica-bearing layer in sample ba15–12. (f) White mica *P*-lines for sample ba14–14 (sedimentary cover). Temperatures are estimated from chlorite in sample ba15–10 (bottom right inset). The top-left inset shows ^{40}Ar/^{39}Ar white mica ages of sample ba14–14 sorted by increasing age.

ca. 200–180 Ma (Airaghi et al., 2018; Huang, Maas, et al., 2003; Weller et al., 2013), lasting over 20 Ma. All the D3 structures observed both in the basement and in the metasedimentary cover are associated with NNE-SSW oriented structures such as F3 folds in the metasedimentary cover and top-to-SE shearing and greenschist facies metamorphic minerals dated at Early Cretaceous (Figure 11c; Airaghi, de Sigoyer, et al.,

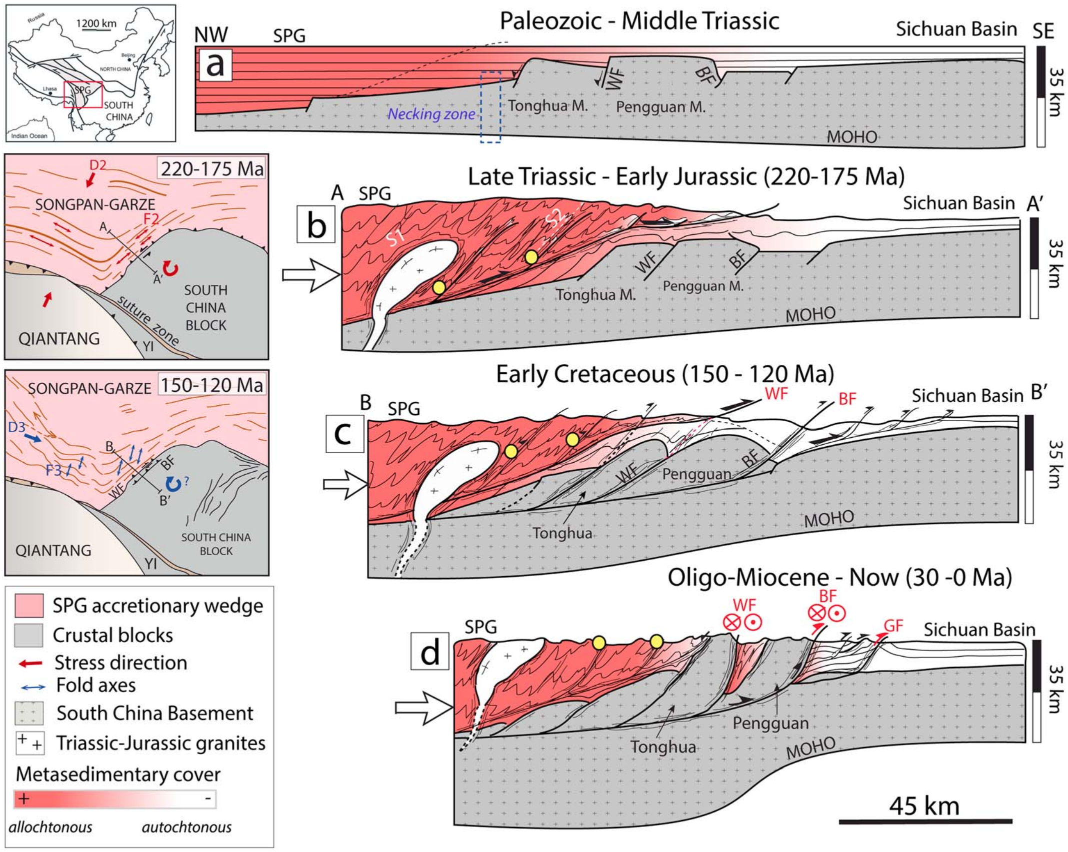

Figure 11. Interpretative cross sections of the tectonic evolution of the Longmen Shan from the Paleozoic to the present. The left insets show a regional view of the geodynamics at each step, evinced from structural observations and from the reconstructions of Roger et al. (2008). The shortening during the Triassic-Jurassic is only qualitative. Yellow dots: position of the highest metamorphic rocks at each stage. White arrows: shortening direction. WF: Wenchuan fault, BF: Beichuan fault, GF: Guanxian fault, SPG: Songpan-Garze, YI: Yidun terrane. (a) Passive margin at the Paleozoic. (b) Late Triassic-Early Jurassic compression and exhumation. The orientation of the D2 structures are regionally compatible with top-to-south thrusting orientation related to the N-S directed closure of the northern branch of the Paleotethys and with the contemporary clockwise rotation of the South China block (inset; e.g., Harrowfield & Wilson, 2005; Q.-R. Meng et al., 2005; Deng, 2007). (c) Early Cretaceous reactivation. The orientation of the structure is regionally compatible with the E-W compression (inset). (d) Schematic cross section of the present structure of the belt. SPG = Songpan-Garze.

2017; Airaghi et al., 2018). These observations deviate from the top-to-NW ductile movement documented in the western part of the Pengguan massif along the WSZ by some previous study (Xu et al., 2008; Xue et al., 2017). Both tectonic dynamics can, however, coexist and be consistent with a southeast thrusting during the Early Cretaceous, resulting in the formation of basement-slice-imbricated structures (Airaghi et al., 2018; Xue et al., 2017; this study). Furthermore, a Cretaceous reactivation is also recorded ~200 km NW of the LMS, in the Longriba fault zone and in the Aba block (Ansberque et al., 2018; Tan et al., 2014), suggesting that a large portion of the eastern Tibet remained coupled during Cretaceous exhumation (Ansberque et al., 2018).

In the external metasedimentary units, two and three phases of ductile deformation are observed east and west of the WSF, respectively. In the Devonian sediments (sample sa14-2) the *P*-*T* conditions of the greenschist facies peak assemblage (4.5 ± 2 kbar, 340 ± 30 °C) are close to the ones of the greenschist facies overprint observed in the internal units, suggesting that in the external domain this late event might be the only recrystallization event. The *P*-*T* conditions at 300 ± 30 °C, 8 ± 1 kbar obtained in the Sinian sediments roofing the Pengguan massif (samples lm230 and lm09-37) are in good agreement with the *P*-*T* estimates obtained for the Pengguan massif (Airaghi, de Sigoyer, et al., 2017). Assuming a density for the crust of 2700 kg/m^3 and the lithostatic pressure hypothesis, these results imply that the Devonian sediments were exhumed from a depth of ~15 km and were partially thickened and detached over the basement (Pengguan massif), while the Sinian sediments experienced a coherent metamorphic history with the

Pengguan massif and were exhumed from ~20-km depth. No ages are yet available for the metamorphic peak in the metasedimentary external units. Structural and sedimentary investigations in the foreland basin indicate, however, that the deformation phase related to thickening reached the front of the LMS by the Late Triassic (e.g., Chen & Wilson, 1995; Li et al., 2003; Li, Yan, et al., 2014; Robert et al., 2011), in agreement with the ZFT at 180 Ma obtained by Arne et al. (1997) at the front of the belt and with the timing of the klippen emplacement (Zheng et al., 2014).

The metamorphic jump between the internal SPG metasedimentary units and the external units and the basement implies the existence of a major decollement between the two domains, at the time of the SPG nappe emplacement (Late Triassic-Early Jurassic, Figures 11b and 11c). Field observations suggest the existence of sub-parallel thrusts within the SPG metasedimentary units contemporaneous with the medium-grade metamorphism, structurally rooted in a decollement (or ductile crustal layer) located in the Silurian schists (at the base of the post-rift sediments). The predominant structural style in the LMS during the Late Triassic-Early Jurassic was therefore thin-skinned (Figure 11b). The record of the only D3 structures in the crystalline basement attest of the onset of the thick-skinned deformation at the Early Cretaceous and the re-activation of the Beichuan and WFs (Figure 11c). The thick-skinned deformation became progressively dominant across the entire central LMS (Figure 11d), as suggested by the recent 2008 Wenchuan earthquake nucleating in a basement fault that partly reactivated as a thrust.

7.2. Structural and *P-T-t* Evolution of the Southern LMS

In the southern LMS, only one major ductile deformation phase is observed and is defined by field structures indicating a top-to-east (top-to-the foreland) shearing associated with greenschist facies metamorphism, in contrast with the Late Cretaceous to Paleogene, top-to-west (top-to-the hinterland) shearing previously proposed (Tian et al., 2016). However, these divergent observations can coexist as documented in the Pengguan massif during the Early Cretaceous (Xue et al., 2017). They are both compatible indeed with a phase of shortening and crustal thickening of the basement and the sedimentary cover. Shortening and crustal thickening stage is also in line with the presence of Late-Cretaceous-early Paleogene basins—interpreted as foreland basins—at the front of the southern part of the belt (Guo et al., 1996) and with the absence of an extensional basin filled with Paleogene sediments in the hanging wall of the major tectonic structures.

P-T conditions of the greenschist facies assemblage in the crystalline rocks (360 ± 30 °C, 6 ± 2 kbar) suggest that the basement in the hanging wall of the WuF was exhumed from ~20-km depth (assuming the lithostatic pressure hypothesis with a crustal density of 2700 kg/m^3), in agreement with the *P-T-z* conditions obtained in the Pengguan and Tonghua massifs (Airaghi, de Sigoyer, et al., 2017; Airaghi et al., 2018). The metasedimentary cover was instead exhumed from ~10-km depth (~3 kbar).

The age of the greenschist facies overprint in the basement of ca. 80–60 Ma is in very good agreement with the ^{40}Ar/^{39}Ar ages obtained by Tian et al. (2016) and with the ^{40}Ar/^{39}Ar biotite ages obtained by Zhou et al. (2008) in the basement of the Danba massif (Figure 12). Hence, in the southern LMS—as in a larger part of the southern margin of the eastern Tibetan plateau—the basement was actively involved into metamorphism and deformation at the Late Cretaceous, while the sedimentary cover records a prolonged deformation event until the Eocene. At this time, the shortening and crustal thickening was possibly triggered by the effects of the India-Asia convergence and the late subduction of the Tethys, first perceived from the southern LMS northwestward to the Danba area, as also suggested by thermochronological data (e.g., Cook et al., 2013; Kirby et al., 2002).

7.3. Tectonic Implications

7.3.1. The Long-Term Thrusting Component of the Major Faults

The fact that the sharpest metamorphic jumps of ~5–6 kbar, 150–200 °C, and ~50 °C observed across the WF and BF, respectively, are Mesozoic in age suggests that these faults were already major active lithospheric boundaries during the Mesozoic. The record of Early Jurassic metamorphism in the internal Tonghua crystalline massif but not in the external Pengguan massif (Airaghi, de Sigoyer, et al., 2017; Airaghi et al., 2018) also indicates that the WF constituted a major tectonic boundary already at that time. The distribution of metamorphic rocks in the central LMS therefore attests of a significant vertical component in the long-term functioning of the BF and WF, with a minimum cumulated vertical offset for the two faults of ~20 km (Airaghi, de Sigoyer, et al., 2017). In the southern LMS the basement is also exhumed from ~20-km depth, attesting of

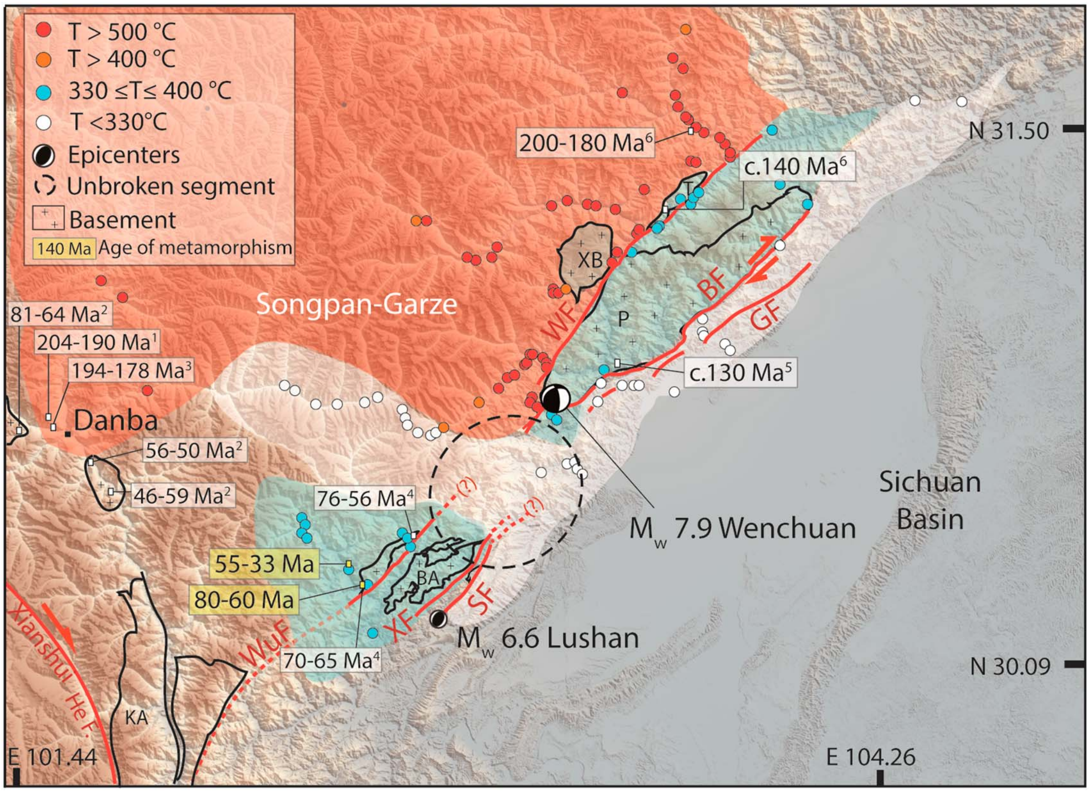

Figure 12. Map of the maximum temperatures experienced by the metasedimentary units along the entire Longmen Shan, from a compilation of newly acquired and previously published (Robert, Pubellier, et al., 2010; Airaghi, Lanari, et al., 2017) RSCM T_{max}. WF: Wenchuan fault, BF: Beichuan fault, GF: Guanxian fault, WuF: Wulong fault, XF: Xiaoguanzi fault, SF: Shuangshi fault, Ka: Kanding. Filled black contours: crystalline massifs (basement). Dashed black circle: unbroken segments between the 2008 M_w 7.9 Wenchuan and 2013 M_w 6.6 Lushan seismic ruptures (e.g., Z. Wang et al., 2015). GS: Greenschist facies metamorphism. Numbers in boxes are ages from this study (yellow) and from literature (white). Ages linked to the crystallization of metamorphic minerals along S2 cleavage during the regional amphibolite-facies metamorphism are as follows: 1: U-Pb monazite and Sm-Nd garnet ages of Huang, Maas, et al. (2003), 2: ^{40}Ar/^{39}Ar amphibole and biotite ages of Zhou et al. (2008), 3: U-Pb monazite ages of Weller et al. (2013), 6: ^{40}Ar/^{39}Ar biotite and U-Pb allanite ages (metasediments) of Airaghi et al. (2018). Ages dating the greenschist facies metamorphism are as follows: 4: ^{40}Ar/^{39}Ar muscovite and biotite ages of Tian et al. (2016), 5: ^{40}Ar/^{39}Ar muscovite ages of Airaghi, de Sigoyer, et al. (2017), 6: ^{40}Ar/^{39}Ar muscovite (basement).

the long-term thrusting movement also of the WuF. Note that the amount of strike-slip component of the deformation during the Late Triassic-Early Jurassic is difficult to evaluate with the petrological approach used in this study and thus must remain, for the present, unquantified.

7.3.2. Continuity Between the WF and BF and Faults of the Southern LMS

Our petrological and structural approach reveals that the BF separates low-grade metamorphic metasedimentary units to the west from non-metamorphic units to the east and favors the exhumation of the basement (Pengguan massif) in its hanging wall (Figure 11d). A similar configuration is observed for the Xiaoguanzi fault in the southern LMS (Figure 9b). These faults might be therefore considered as structurally equivalent. By contrast, the WF corresponds (1) to a Late Triassic-Early Jurassic zone of decollement separating the medium-grade metasedimentary units from the base of SPG series to the west (internal units) and the low-grade metasedimetary units to the east (external units) where the basement is not exhumed or (2) to the tectonic boundary that limits the slices of the basement without any major metamorphic jump, where the basement is exhumed (e.g., Tonghua massif; Figures 9a and 11d). Using a petrological approach, it is therefore possible to distinguish the SPG decollement level responsible for the metamorphic jump between internal and external units from the WF sensu stricto that favors the exhumation of the basement in its hanging wall. In the southern LMS, the WuF—often considered as the southern prolongation of the WF—also favors the exhumation of the basement in its hanging wall, but it never corresponds to the limit between different metamorphic domains. Hence, the WuF cannot be considered as the southern prolongation of the SPG decollement level. This level may instead deviate from the central LMS westward, to join the Danba dome where medium-grade metamorphic rocks are exhumed (e.g., Billerot et al., 2017; Weller et al., 2013). The petrochronological approach thus allows to better define the WF zone and its petrological significance.

7.3.3. Different Tectonometamorphic Evolutions for the Central and Southern LMS

Structural and petrochronological data show that different tectonometamorphic features are observed between the central and southern LMS. The metasedimentary cover of the southern area does not clearly record, for example, three stages of ductile deformation as observed in the central areas. Furthermore, the *P-T* conditions of the metasedimentary cover in the south are close to the ones observed in the external units of the central LMS but the amphibolite-facies metamorphism that characterizes the internal units of the central LMS is not observed in the south (Figure 12). This suggests that the southern LMS never experienced the overthrusting of the thickened SPG units toward the external part of the belt. The different metamorphic domains (blue and red in Figure 12) of the central and southern LMS are separated by a 30- to 40-km-wide area where no metamorphic rocks are observed ($T \ll 330$ °C, white in Figure 12). This non-metamorphic zone extends from the front of the belt, westward within the SPG terrain and corresponds to the area where zircon fission track ages have not been reset since the Triassic (Tan et al., 2014). Deep metamorphic units were therefore never exhumed within this area.

Differences in the timing of metamorphism between the central and southern LMS are also observed. While in the south the greenschist facies metamorphic event affecting the basement is younger than 80 Ma (yellow boxes in Figure 12), in the central LMS it is dated at 140–120 Ma (white boxes in Figure 12). This suggests that while the central LMS experienced a phase of thickening and exhumation during the Early Cretaceous, the southern LMS did not, or the Early Cretaceous event is there completely overprinted by the Cenozoic history. During the Cenozoic, the central LMS was therefore already at a higher structural level (below closure *T* of ZFTs) while the southern LMS experienced thickening and deformation. This is consistent with the stratigraphic record in the foreland Sichuan basin showing a migration of the depocenter northward during the Early Cretaceous and southward during the Cenozoic (e.g., Burchfiel et al., 1995; Q.-R. Meng et al., 2005). Hence, the central and southern LMS underwent different tectonometamorphic histories since the Early Mesozoic, that results in an along-strike metamorphic segmentation of the belt. Different portions of the belt were therefore re-activated at different times, maybe due to a difference in the maturation of the associated fault systems.

7.3.4. Implications for the Present Tectonics

The relocation of the recent earthquake epicenters shows that the 2008 M_w 7.9 Wenchuan and 2013 M_w 6.6 Lushan earthquakes (green stars in Figure 12) nucleated in areas where the crystalline basement crops out (filled black lines in Figure 12). The epicenters are separated by an as-yet unbroken segment, where recent earthquakes did not propagate, whose size broadly corresponds to the size of the area where no metamorphic rocks are observed (dashed black line and white area in Figure 12). This metamorphic segmentation might be controlled by tectonic structures (possibly inherited from the Paleozoic passive margin of the South China craton) that—on the base of the contours of metamorphic discontinuities—should be SE-NW oriented, subparallel to the Xianshui He fault. The lateral ramp of the RFBT (below the Shuangshi fault) that limited the propagation of the Lushan earthquake northeastward into the unbroken segment (Li, Jia, et al., 2014) might represent one of these structures. Inherited structures responsible for the along-strike metamorphic segmentation in the LMS might therefore still affect the present dynamics. They might also partially explain the present crustal structure of the belt imaged by seismic tomography at ~ 20 km depth (Z. Wang et al., 2015). Our tectono-metamorphic approach thus offers new and complementary constraints to understand the importance of the Mesozoic geological inheritance in the present tectonics of the LMS.

8. Conclusions

1. New petrological observations in the central LMS show a metamorphic jump of ~50 °C (~3 kbar) across the BF. A second metamorphic jump is observed across the SPG decollement zone (locally superposed to the WF) of ~150–200 °C, 5–6 kbar between the metasedimentary rocks of the internal units of the central LMS ($T > 500$ °C) and metasedimentary rocks in the external units of the belt ($T < 400$ °C). The SPG decollement limiting the different metamorphic provinces can therefore be distinguishing from the WF sensu stricto that favors the exhumation of the Xuelongbao and Tonghua crystalline massifs in its hanging wall and across which no major metamorphic jumps are observed.

2. The metamorphic jumps across the Beichuan, Wenchuan, and the SPG decollement zone attest to their long-term thrusting components and show that they already constituted major crustal boundaries from the Late Triassic-Early Jurassic.
3. In the internal metasedimentary units of the central LMS three phases of ductile deformation are observed: D1, D2 related to top-to-SE shearing, and D3 related to top-to-E shearing. In the southern LMS only one major ductile deformation phase related to top-to-ESE shearing is observed.
4. The equilibrium *P-T* conditions of the greenschist metamorphic assemblage in the external units of the central LMS yield at 300 ± 30 °C, 7−8 ± 1 kbar in the Sinian sediments remained attached to the Pengguan crystalline massif and at 340 ± 30 °C, 4.5 ± 2 kbar in the paraautochthonous Devonian sediments.
5. No higher than greenschist facies metamorphic conditions were reached in the basement and in the metasedimentary cover of the southern LMS. Peak conditions of 360 ± 30 °C and 6 ± 2 kbar were reached at ca. 80–58 Ma in the basement and 350 ± 30 °C, 3 ± 1 kbar at ca. 55–33 Ma in the metasedimentary cover.
6. In the long term, the WuF cannot be considered in continuity with the SPG decollement zone separating the internal and external units in the central LMS.
7. The first comprehensive maps of paleotemperatures for the entire LMS shows an along-strike metamorphic segmentation between the central and southern LMS. The amphibolite facies metamorphism related to the thickening and thrusting of the SPG metasedimentary rocks is only observed in the central LMS, while the greenschist facies overprint observed in the basement is dated at ca. 140–120 Ma in the central LMS and <80 Ma in the southern LMS. The central and southern LMS therefore underwent different tectonometamorphic histories since the Mesozoic maybe due to differences in the maturation of the associated fault systems.
8. The metamorphic segmentation and the geographic distribution of the outcropping basement seem to mime the locations of the recent earthquake epicenters, while the area where no long-term exhumation is observed well corresponds to the width of the unbroken segment where the rupture did not propagate. The inherited structures responsible for the long-term along-strike metamorphic segmentation might therefore still affect the present tectonics of the belt. Farther investigations on the reasons of the metamorphic segmentation are now required.

Acknowledgments

The project was made possible by the financial support of Agence Nationale de la Recherche (ANR) AA-PJCJC SIMI5-6 LONGRIBA and ANR-13-BS06-012-01 DSP-Tibet, the INSU-CNRS and LabEx "OSUG@2020". We acknowledge the anonymous reviewers for their constructive comments. We thank Laetitia Lamrabet for her work with the RSCM technique. We also thank Tan Xibin (China Earthquake Administration), Professor Xu Xiwei (China Earthquake Administration), Professor Li Yong (Chengdu University of Technology), and students from both universities, for their logistical support in the field and scientific discussions. We also acknowledge Valérie Magnin and Valentina Batanova for support with EPMA facilities. We thank Gilles Montagnac and the Raman Spectroscopy National Facility of the ENS Lyon for their support with the RSCM analyses. A table with the RSCM temperatures, the procedure for ^{40}Ar/^{39}Ar white mica dating, and a table with the ^{40}Ar/^{39}Ar analytical results can be found in the supporting information.

References

Airaghi, L., de Sigoyer, J., Lanari, P., Guillot, S., Vidal, O., Monié, P., et al. (2017). Total exhumation across the Beichuan fault in the Longmen Shan (eastern Tibetan plateau, China): Constraints from petrology and thermobarometry. *Journal of Asian Earth Sciences*, *140*, 108–121. https://doi.org/10.1016/j.jseaes.2017.04.003

Airaghi, L., Lanari, P., de Sigoyer, J., & Guillot, S. (2017). Microstructural vs compositional preservation and pseudomorphic replacement of muscovite in deformed metapelites from the Longmen Shan (Sichuan, China). *Lithos*, *282-283*, 260–280.

Airaghi, L., Warren, C. J., de Sigoyer, J., Lanari, P., & Magnin, V. (2018). Influence of dissolution/reprecipatation reactions on metamorphic greenschist to amphibolite facies mica ^{40}Ar/^{39}Ar ages in the Longmen Shan (eastern Tibet). *Journal of Metamorphic Geology*, *36*(7), 933–958. https://doi.org/10.1111/jmg.12420

Ansberque, C., Godard, V., Olivetti, V., Bellier, O., de Sigoyer, J., Bernet, M., et al. (2018). Differential Exhumation across the Longriba Fault System: Implications for the Eastern Tibetan Plateau. *Tectonics*, *37*, 663–679. https://doi.org/10.1002/2017TC004816

Arne, D., Worley, B., Wilson, C., Che, S., Foster, D., Luo, Z., et al. (1997). Differential exhumation in response to episodic thrusting along the eastern margin of the Tibetan Plateau. *Tectonophysics*, *280*(3–4), 239–256. https://doi.org/10.1016/S0040-1951(97)00040-1

Beyssac, O., Rouzaud, J.-N., Goffé, B., Brunet, F., & Chopin, C. (2002). Graphitization in a high-pressure, low-temperature metamorphic gradient: A Raman microspectroscopy and HRTEM study. *Contributions to Mineralogy and Petrology*, *143*(1), 19–31.

Billerot, A., Duchene, S., Vanderhaeghe, O., & de Sigoyer, J. (2017). Gneiss domes of the Danba metamorphic complex, Songpan Ganze, eastern Tibet. *Journal of Asian Earth Sciences*, *140*, 48–74.

Burchfiel, B., Chen, Z., Liu, Y., & Royden, L. (1995). Tectonics of the Longmen Shan and adjacent regions, central China. *International Geology Review*, *37*, 661–735.

Calassou, S. (1994). Etude tectonique d'une chane de dcollement: (a) tectonique triasique et tertiaire de la chaîne de Songpan-Garze. (b) géometrie et cinmatique des déformations dans les prismes d'accrétion sédimentaires: modélisation analogique (PhD thesis). Université de Montpellier II.

Chen, S. F., & Wilson, C. (1995). Emplacement of the Longmen Shan Thrust-Nappe Belt along the eastern margin of the Tibetan plateau. *Journal of Structural Geology*, *18*, 413–430.

Cook, K., Royden, L., Burchfiel, B., Lee, Y.-H., & Tan, X. (2013). Constraints on Cenozoic tectonics in the southwestern Longmen Shan from low-temperature thermochronology. *Lithosphere*, *5*(4), 393–406.

de Michele, M., Raucoules, D., Lasserre, C., Pathier, E., Klinger, Y., Vand Der Woerd, J., et al. (2010). The *Mw* 7.9, 12 May 2008 Sichuan earthquake rupture measured by sub-pixel correlation of ALOS PALSAR amplitude images. *Earth, Planets and Space*, *62*(11), 875–879. https://doi.org/10.5047/eps.2009.05.002

de Sigoyer, J., Billerot, A., Duchene, S., Vanderhaeghe, O., Pubellier, M., & Monié, P. (2011). How the paradoxal Longmen Shan belt has been built: Through new petrological structural geochronological data? *Journal of Himalayan Earth Sciences*, *44*(1), 10–12.

de Sigoyer, J., Vanderhaeghe, O., Duchene, S., & Billerot, A. (2014). Generation and emplacement of Triassic granitoids within the Sonpan Ganze accretionary-orogenic wedge in a context of slab retreat accommodated by tear faulting, Eastern Tibetan plateau, China. *Journal of Asia Earth Sciences*, *88*, 192–216.

Deng, K. L. (2007). Indosinian progressive deformation and its chronogenesis in Longmengshan structural belt. *Oil & Gas Geology*, *28*(4), 485–490.

Densmore, A., Ellis, M., Li, Y., Zhou, R., Hancock, G., & Richardson, N. (2007). Active tectonics of the Beichuan and Pengguan faults at the eastern margin of the Tibetan plateau. *Tectonics*, *26*, TC4005. https://doi.org/10.1029/2006TC001987

Deschamps, F., Duchene, S., de Sigoyer, J., Bosse, V., Benoit, M., & Vanderhaeghe, O. (2018). Coeval mantle-derived and crust-derived magmas forming two neighbouring plutons in the Songpan Ganze accretionary orogenic wedge (SW China). *Journal of Petrology*. https://doi.org/10.1093/petrology/egy007

Dirks, P., Wilson, C., Chen, S., Luo, Z., & Liu, S. (1994). Tectonic evolution of the NE margin of the Tibetan plateau; evidence from the central Longmen Mountains, Sichuan Province, China. *Journal of Southeast Asian Earth Sciences*, *9*, 181–192.

Dubacq, B., Vidal, O., & De Andrade, V. (2010). Dehydration of dioctahedral aluminous phyllosilicates: thermodynamic modelling and implications for thermobarometric estimates. *Contributions to Mineralogy and Petrology*, *159*, 159–174.

Godard, V., Pik, R., Lavé, J., Cattin, R., Tibari, B., de Sigoyer, J., et al. (2009). Late Cenozoic evolution of the central Longmen Shan, eastern Tibet: Insight from (U-Th)/He thermochronometry. *Tectonics*, *28*, TC5009. https://doi.org/10.1029/2008TC002407

Guo, Z., Deng, K., & Han, Y. (1996). *Formation and evolution of the Sichuan basin*. Beijing: Geological Publishing House.

Harrison, T. M., Célérier, J., Aikman, A. B., Hermann, J., & Hizler, M. T. (2009). Diffusion of ^{40}Ar in muscovite. *Geochimica et Cosmochimica Acta*, *73*, 1039–1051.

Harrowfield, M. J., & Wilson, C. J. L. (2005). Indosinian deformation of the Songpan Garze fold belt, northeast Tibetan plateau. *Journal of Structural Geology*, *27*, 101–117.

Huang, M., Maas, R., Buick, I. S., & Williams, I. S. (2003). Crustal response to continental collisions between the Tibet, Indian, South China and North China blocks: Geochronological constraints from the Songpan-Garze Orogenic Belt, western China. *Journal of Metamorphic Geology*, *21*(3), 223–240.

Huang, M.-H., Bürgmann, R., & Freed, A. M. (2014). Probing the lithospheric rheology across the eastern margin of the Tibetan Plateau. *Earth and Planetary Science Letters*, *396*, 88–96.

Hubbard, J., & Shaw, J. (2009). Uplift of the Longmen Shan and Tibetan plateau, and the 2008 Wenchuan (M = 7.9) earthquake. *Nature Letters*, *28*, 1032–1047.

Hubbard, J., Shaw, J., & Klinger, Y. (2010). Structural setting of the 2008 *Mw* 7.9 Wenchuan, China, earthquake. *Bulletin of the Seismological Society of America Letters*, *100*(5B), 2713–2735.

Jia, D., Wei, G., Chen, Z., Li, B., Zeng, Q., & Yang, G. (2006). Longmen Shan fold-thrust belt and its relation to the western Sichuan Basin in central China: New insights from hydrocarbon exploration. *AAPG Bulletin*, *90*(9), 1425–1447.

Jiang, X., & Jin, Y. (2005). Mapping the deep lithospheric structure beneath the eastern margin of the Tibetan plateau from gravity anomalies. *Journal of Geophysical Research*, *110*, B07407. https://doi.org/10.1029/2004JB003394

Kapp, P., De Celles, P. G., Gehrels, G. E., Heizler, M., & Ding, L. (2007). Geological records of the Lhasa-Qiangtang and Indo-Asian collision in the Nima area of central Tibet. *Geological Society of America Bulletin*, *119*(7–8), 917–933.

Kapp, P., Murphy, M. A., Yin, A., Harrison, T. M., Ding, L., & Guo, J. (2003). Mesozoic and Cenozoic tectonic evolution of the Shiquanhe area of western Tibet. *Tectonics*, *22*(4), 1029. https://doi.org/10.1029/2001TC001332

Kirby, E., Reiners, P., Krol, M., Hodges, K., Whipple, K., Farley, K., et al. (2002). Late Cenozoic uplift and landscape evolution along the eastern margin of the Tibetan Plateau: Inferences from ^{40}Ar/^{39}Ar and (U-Th)/He thermocronology. *Tectonics*, *21*(1), 1001. https://doi.org/10.1029/2000TC001246

Lanari, P., Guillot, S., Schwartz, S., Vidal, O., Tricart, P., Riel, N., & Beyssac, O. (2012). Diachronous evolution of the alpine continental subduction wedge: Evidence from *P-T* estimates in the Brianconnais Zone houillere (France - Western Alps). *Journal of Geodynamics*, *56-57*, 39–54.

Lanari, P., Vidal, O., De Andrade, V., Dubacq, B., Lewin, E., Grosch, E., & Schwartz, S. (2014). XMapTools: A MATLAB-based program for electron microprobe X-ray imcage processing and geothermobarometry. *Computers & Geosciences*, *62*, 227–240.

Li, Y., Allen, P. A., Densmore, A. L., & Qiang, X. (2003). Evolution of the Longmen Shan foreland basin (Western Sichuan, China) during the Late Triassic Indosinian orogeny. *Basin Research*, *15*(1), 117–138.

Li, Y., Jia, D., Wang, M., Shaw, J. H., He, J., Lin, A., et al. (2014). Structural geometry of the source region for the 2013 Mw 6.6 Lushan earthquake: Implication for earthquake hazard assessment along the Longmen Shan. *Earth and Planetary Science Letters*, *390*, 275–286.

Li, Y., Li, H., Zhou, R., Su, D., Yan, L., & Yan, Z. (2014). Crustal thickening or isostatic rebound of orogenic wedge deduced from tectonostratigraphic units in Indosinian foreland basin, Longmen Shan, China. *Tectonophysics*, *619-620*, 1–12.

Li, Y., Yan, Z., Liu, S., Li, H., Cao, J., Su, D., et al. (2014). Migration of the carbonate ramp and sponge buildup driven by the orogenic wedge advance in the early stage (Carnian) of the Longmen Shan foreland basin, China. *Tectonophysics*, *619-620*, 179–193.

Liao, T.-P., Hu, J.-J., Zhang, F.-R., Chen, H.-K., & Sun, H.-Q. (2009). Relation between structural evolution of the Longmen Shan orogenic zone and sedimentation of its foreland basin. *Mining Science and Technology (China)*, *19*(6), 807–812.

Lichun, C., Hu, W., Yongkang, R., Shengxue, L., Xi, L., Fuyao, W., et al. (2014). The 2013 Lushan Ms 7.0 earthquake: varied seismogenic structure from the 2008 Wenchuan earthquake. *Seismological Research Letters*, *85*(1), 34–39. https://doi.org/10.1785/0220130109

Liu, C., Zheng, Y., Ge, C., Xiong, X., & Hsu, H. (2013). Rupture process of the *Ms* 7.0 Lushan earthquake, 2013. *Science China Earth Sciences*, *56*, 1187–1192.

Massonne, H., & Schreyer, W. (1987). Phengite geobarometry based on the limiting assemblage with K-feldspar, phlogopite, and quartz. *Contributions to Mineralogy and Petrology*, *96*, 212–224.

Meng, E., Liu, F.-L., Du, L.-L., Liu, P.-H., & Liu, J.-H. (2015). Petrogenesis and tectonic significance of the Baoxing granitic and mafic intrusions, southwestern China: Evidence from zircon U-Pb dating and Lu-Hf isotopes, and whole-rock geochemistry. *Gondwana Research*, *28*(2), 800–815.

Meng, Q.-R., Wang, E., & Hu, J.-M. (2005). Mesozoic sedimentary evolution of the northwest Sichuan basin: Implication for continued clockwise rotation of the South China block. *GSA Bulletin*, *117*(3–4), 396–410.

Passchier, C., & Trouw, R. (2005). *Microtectonics*. Berlin Heidelberg: Spinger-Verlag.

Robert, A. (2011). Déformation polyphasée et importance de l'héritage structural dans les Longmen Shan (Sichuan, Chine). Apport d'une approche couplée entre géophysique et géologie (PhD thesis). Université de Paris Sud 11.

Robert, A., Pubellier, M., de Sigoyer, J., Lanari, P., Vergne, J., Vidal, O., & Bosse, V. (2011). Crustal-scale deformation history of the Longmen Shan polyphased range located at the eastern border of the Tibetan plateau. *Journal of Himalaya Earth Sciences*, *44*(1), 68–69.

Robert, A., Pubellier, M., de Sigoyer, J., Vergne, J., Lahfid, A., Cattin, R., et al. (2010). Structural and thermal characters of the Longmen Shan (Sichuan, China). *Tectonophysics*, *491*(1–4), 165–173. https://doi.org/10.1016/j.tecto.2010.03.018

Robert, A., Zhu, J., Vergne, J., Cattin, R., Chan, L., Wittlinger, G., et al. (2010). Crustal structures in the area of the 2008 Sichuan earthquake from seismologic and gravimetric data. *Tectonophysics*, *491*(1–4), 205–210. https://doi.org/10.1016/j.tecto.2009.11.010

Roger, F., Jolivet, M., & Malavieille, J. (2008). Tectonic evolution of the Triassic fold belts of Tibet. *Comptes Rendus Geosciences*, *340*, 180–189.

Roger, F., Jolivet, M., & Malavieille, J. (2010). The tectonic evolution of the Songpan-Garzê (North Tibet) and adjacent areas from Proterozoic to Present: A synthesis. *Journal of Asia Earth Sciences*, *39*, 254–269.

Roger, F., Malavieille, J., Leloup, P., Calassou, S., & Xu, Z. (2004). Timing of granite emplacement and cooling in the Songpan-Garzê fold belt (eastern Tibetan Plateau) with tectonic implications. *Journal of Asian Earth Science*, *22*, 465–481.

SBGMR (Sichuan Bureau of Geology and Mineral Resources) (1991). *Regional Geology of Sichuan Province* (728 pp.). Beijing: Geological Publishing House.

Stipp, M., Stünitz, H., Heilbronner, R., & Schmid, S. M. (2002). The eastern Tonale fault zone: A 'natural laboratory' for crystal plastic deformation of quartz over a temperature range from 250 to 700°C. *Journal of Structural Geology*, *24*, 1861–1884.

Tan, X., Lee, Y., Chen, W., Cook, K., & Xu, X. (2014). Exhumation history and faulting activity of the southern segment of the Longmen Shan, eastern Tibet. *Journal of Asian Earth Sciences*, *81*, 91–104.

Tan, X.-B., Xu, X.-W., Lee, Y.-H., Lu, R.-Q., Liu, Y., Xu, C., et al. (2017). Late Cenozoic thrusting of major faults along the central segment of Longmen Shan, eastern Tibet: Evidence from low-temperature thermochronology. *Tectonophysics*, *712-713*, 145–155. https://doi.org/10.1016/j.tecto.2017.05.016

Tian, Y., Kohn, B. P., Philipps, D., Hu, S., Gleadow, A. J. W., & Carter, A. (2016). Late Cretaceous-earliest Paleogene deformation in the Longmen Shan fold-and-thrust belt, eastern Tibetan plateau margin: Pre-Cenozoic thickened crust? *Tectonics*, *35*, 2293–2312. https://doi.org/10.1002/2016TC004182

Vidal, O., De Andrade, V., Lewin, E., Munoz, M., Parra, T., & Pascarelli, S. (2006). P-T deformation-Fe3+/Fe2+ mapping at the thin section scale and comparison with XANES mapping. Application to a garnet-bearing metapeite from Sambagawa metamorphic belt (Japan). *Journal of Metamorphic Geology*, *24*, 669–683.

Vidal, O., Parra, T., & Vieillard, P. (2005). Thermodynamic properties on the Tschermak solid solution in Fe-chlorite: Application to natural examples and possible role of oxidation. *American Mineralogist*, *90*, 347–358.

Wang, E., Kirby, E., Furlong, K., van Soest, M., Xu, G., Shi, X., et al. (2012). Two-phase growth of high topography in eastern Tibet during the Cenozoic. *Nature Geoscience*, *5*(9), 640–645. https://doi.org/10.1038/ngeo1538

Wang, E., Meng, K., Su, Z., Meng, Q., Chu, J. J., Chen, Z., et al. (2014). Block rotation: Tectonic response of the Sichuan basin to the southeastward growth of the Tibetan plateau along the Xianshuihe-Xiaojiang fault. *Tectonics*, *33*, 686–718. https://doi.org/10.1002/2013TC003337

Wang, Z., Su, J., Liu, C., & Cai, X. (2015). New insights into the generation of the Lushan earthquake (*Ms* 7.0), China. *Journal of Geophysical Research: Solid Earth*, *120*, 3507–3526. https://doi.org/10.1002/2014JB011692

Weller, O. M., St-Onge, M. R., Waters, D. J., Rayner, N., Searle, M. P., Chung, S.-L., et al. (2013). Quantifying Barrovian metamorphism in the Danba structural culmination of eastern Tibet. *Journal of Metamorphic Geology*, *31*(9), 909–935. https://doi.org/10.1111/jmg.12050

Whitney, D. L., & Evans, B. W. (2010). Abbreviations for names of rock-forming minerals. *American Mineralogist*, *95*(1), 185–187.

Worley, B. A., & Wilson, C. J. (1996). Deformation partitioning and foliation reactivation during transpressional orogenesis, an example from the central Longmen Shan, China. *Journal of Structural Geology*, *18*(4), 395–411.

Xu, X., Wen, X., Yu, G., Chen, G., Klinger, Y., Hubbard, J., & Shaw, J. (2009). Coseismic reverse- and oblique-slip surface faulting generated by the 2008 *Mw* 7.9 Wenchuan earthquake, China. *Geology*, *37*(6), 515–518.

Xue, Z., Martelet, G., Lin, W., Faure, M., Chen, Y., Wei, W., et al. (2017). Mesozoic Crustal thickening of the Longmenshan belt (NE Tibet, China) by imbrication of basement slices: Insights from structural analysis, petrofabric and magnetic fabric studies, and gravity modeling. *Tectonics*, *36*, 3110–3134. https://doi.org/10.1002/2017TC004754

Xu, Z. Q., Ji, S. C., Li, H. B., Hou, L. W., Fu, X. F., & Cai, Z. H. (2008). Uplift of the Longmen Shan range and the Wenchuan earthquake. *Episodes*, *31*(3), 291–301.

Yan, D., Zhou, M., Wei, G., Liu, H., Dong, T., Zhang, W., & Jin, Z. (2008). Collapse of Songpan-Garze orogenic belt resulted from Mesozoic middle-crustal ductile channel flow: Evidence from deformation and metamorphism within Sinian-Paleozoic strata in hinterland of Longmenshan Foreland thrust belt. *Earth Science Frontiers*, *15*(3), 186–198.

Yan, D.-P., Zhou, M.-F., Li, S.-B. & Wei, G.-Q. (2011). Structural and geochronological constrains on the Mesozoic-Cenozoic tectonic evolution of the Longmen Shan thrust belt, eastern Tibetan Plateau.

Zhang, H., Oskin, M. E., Liu-Zeng, J., Zhang, P., Reiners, P. W., & Xiao, P. (2016). Pulsed exhumation of interior eastern Tibet: Implications for relief generation mechanisms and the origin of high-elevation planation surfaces. *Earth and Planetary Science Letters*, *449*, 176–185.

Zhang, H., Zhang, P., Yin, J., Lui, C., & Yu, G. (2011). Along-strike topographic variation of the Longmen Shan and its significance for landscape evolution along the eastern Tibetan Plateau. *Journal of Asian Earth Sciences*, *40*(4), 855–864.

Zhang, Z., Wang, Y., Chen, Y., Houseman, G., Tian, X., Wang, E., & Teng, J. (2009). Crustal structure across the Longmenshan fault belt from passive source seismic profiling. *Geophysical Research Letters*, *292*, L17310. https://doi.org/10.1029/2009GL039580

Zhang, Z., Yuan, X., Chen, Y., Tian, X., Kind, R., Li, X., & Teng, J. (2010). Seismic signature of the collision between the East Tibetan escape ow and the Sichuan Basin. *Earth and Planetary Science Letters*, *292*, 254–264.

Zheng, Y., Kong, P., & Fu, B. (2014). Time constraints on the emplacement of klippen in the Longmen Shan thrust belt and tectonic implications. *Tectonophysics*, *634*, 44–54.

Zheng, Y., Li, H., Sun, Z., Wang, H., Zhang, J., Li, C., & Cao, Y. (2016). New geochronology constraints on timing and depth of the ancient earthquakes along the Longmen Shan fault belt, eastern Tibet. *Tectonics*, *35*, 2781–2806. https://doi.org/10.1002/2016tc004210

Zhou, M.-F., Yan, D.-P., Vasconcelos, P. M., Li, J.-W., & Hu, R.-Z. (2008). Structural and geochronological constraints on the tectono-thermal evolution of the Danba domal terrane, eastern margin of the Tibetan plateau. *Journal of Asian Earth Sciences*, *33*, 414–427.

Zhou, M.-F., Yan, D.-P., Wang, C.-L., Qi, L., & Kennedy, A. (2006). Subduction-related origin of the 750 Ma Xuelongbao adakitic complex (Sichuan province, China): Implications for the tectonic setting of the giant Neoproterozoic magmatic event in South China. *Earth and Planetary Science Letters*, *248*(12), 286–300.